Advanced Steel Construction – Vol. 21 No. 4 (2025) 277–293
DOI:10.18057/IJASC.2025.21.4.1

LATERAL DYNAMIC RESPONSES OF GFRP TUBE CONCRETE-ENCASED STEEL COMPOSITE COLUMN WITH FIXED ENDS

Hai-Xia Zhang * and Shi-Long Ju

School of Civil Engineering, Shenyang Jianzhu University, Shenyang 110168, China
** (Corresponding author: E-mail: zhanghaixia@sjzu.edu.cn)*

ABSTRACT

In this study, a finite element (FE) model of a GFRP tube concrete-encased steel composite column (GTCES) with fixed ends was established to investigate its dynamic behavior under vehicle collisions, with the accuracy of the FE results was verified and calibrated by comparisons with the experimental results. The impact force, lateral displacement, local indentation, reaction and inertia force, bending moment and shear force, energy absorption, damage evolution and failure model, and GFRP tube confinement effect were analyzed, with the results illustrating that the impact process can be divide into three stage. Concrete is an important factor in carrying the impact loads. Subsequently, the influences of the axial force ratio, concrete strength, encased steel yield strength, steel ratio, and impact velocity on the dynamic behavior of the GTCES columns were investigated using parametric experiments. The findings revealed that the peak local indentation decreased by 22.78% and the peak impact force increases by 19.49%, respectively, with increasing the axial force ratio from 0 to 0.6. When the strength of concrete increased from 30 MPa to 40 MPa, the decreases of peak and residual lateral displacements were 23.91% and 25.89%, respectively. Additionally, the more severe damage on the GTCES column was observed at the higher impact velocities.

ARTICLE HISTORY

Received: 31 October 2024
Revised: 4 January 2025
Accepted: 8 January 2025

KEYWORDS

Impact response;
Finite element model;
GFRP tube;
Concrete-encased steel column

1. Introduction

Fiber-reinforced polymer (FRP) composites have been applied in civil engineering due to their exceptional material qualities, which include high strength, superior corrosion resistance, and low self-weight [1-3]. One wide application is that the FRP composites as tubes combined with steel and concrete to develop new composite constructions, such as FRP-concrete steel double-skin tubular columns (DSTCs) [4-8], concrete-filled in FRP tubes with longitudinal steel bars and FRP-confined concrete-filled steel tubes(CCFTs) [9-12]. The FRP tube serves as a formwork during concrete pouring, and provide a corrosion-resistant skin to protect core concrete from corrosion when the composite construction serves in corrosive engineering environments. Furthermore, the FRP tubes serve as a confinement system that enhances the mechanical properties of the concrete [13,14].

Simultaneously, GFRP tube concrete-encased steel composite columns (GTCES), a novel form of hybrid columns [15], are prepared by surrounding the encased steel with an outer GFRP tube, which is then filled with concrete. The concept of the GTCES column was proposed by Liu, as a rehabilitation technique for strengthening the corroded steel members [16]. The corroded steel members were enclosed by two semi-circular GFRP tubes, which were then filled with lightweight expanded concrete. An axial compressive test was conducted on the composite columns. The composite columns exhibited suitable mechanical properties. Since then, a few investigations have been conducted on the composite column [17-22]. The investigations revealed that the GTCES column had a superior mechanical performance under static and seismic loading conditions. And axial, flexural and eccentric carrying ability calculation methods and hysteretic restoring force models were proposed for GTCES columns [17,20,22,23]. Thus, GTCES columns have promising applications in vital members such as buildings and bridges.

With the increase in transport accidents, the composite columns may be exposed to impact loads from vehicles while in the service. When accidents happen, the composite columns is destroyed, causing the structural collapse and posing a threat to life safety. Recently, the dynamic behaviors of hybrid composite columns with FRP tubes have been studied. Pham et al. [24] used the drop weight tests on a CFTs column to research its axial impact performance. These findings presented that the mechanical resistance of columns could be enhanced by the outer FRP tube confinement effect. Meanwhile, the axial impact performance of the CFTs column with inner steel spiral reinforcement was studied by Huang [25]. The results showed that the inner steel spiral reinforcement improved damage resistance of the CFTs. The lateral dynamic performance of the CFTs was also investigated. Wang et al. [26] studied the lateral dynamic behaviors of CFTs. They found that the peak displacement of the column decreased with increasing fiber volume fraction of FRP tubes, due to the confinement effect of FRP tube was enhanced. Chen et al. [27] also found that improving the confinement effect of FRP tube would lead to a reduction in maximum displacement of CFTs. Furthermore, the impact resistance of CFTs would be improved with embedding the steel spiral reinforcement [28]. Simultaneously, the lateral dynamic performance of DSTCs was investigated and the main parameters analysis were conducted. Chen et al. [27] tested and numerically simulated DSTCs under the lateral impact loads. These findings indicated that the DSTCs exhibited a higher impact resistance with increasing the thickness of FRP tube. Abdelkarim et al. [29,30] established the numerical simulation models for DSTCs under vehicle collisions to study its dynamic responses. The results demonstrated that the main resistance of DSTCs came from inner steel tube and dynamic resistance were affected by the mass and velocity of impactor. Wang et al. [31] carried out the test investigations on the DSTCs members to explore their dynamic responses. The findings demonstrated that the impact resistance of DSTCs was significantly influenced by the impact velocity. Furthermore, the numerical simulation models were established according to test results [31], and the numerous parameter studies were analyzed [32]. Zhang et al. [33] studied the response of DSTCs members under impact load. The results revealed that the specimens presented flexural failure and that a large void ratio decreased the maximum displacement of members. In summary, the previous investigations mainly concentrated on the static and seismic responses of the GTCES column and the dynamic behaviors of the CFFs and DSTc members. However, the investigations on the impact performance of GTCES columns were limited under vehicle collision conditions, thus making it essential to reveal its dynamic behaviors.

In this study, the finite element models of the GTCES columns with fixed-ends were developed to explore their dynamic behavior under vehicle collisions. The simulation results were verified. Subsequently, to reveal the mechanical characteristics, failure modes, the role of each component of GTCES column, the valid model was employed to perform an analysis on the impact process, inertial force, the distribution of bending moment and shear force, the change rule of energy dissipation, damage evolution and failure modes and the GFRP tube confinement effect were discussed in detailed. Finally, the influences of several parameters such as axial force ratio, concrete strength, encased steel strength, steel ratio and impact velocity were analyzed to clarify the main parameters affecting on the lateral impact performance. This study provides a reference to develop the numerical model of GTCES under the dynamic load and reveals its dynamic behaviors. The results offer a reference for anti-impact designs and reinforcement maintenance.

2. Validation of numerical simulation techniques

2.1. Exiting experiments

The experiments in Ref. [31] were selected to calibrate the accuracy of the finite element models of the GTCES under lateral impact. The material components of the specimens were FRP tube, concrete and steel, that were identical to the GTCES columns. Furthermore, the dynamic performance of the GTCES un-

der an axial load was studied. The experimental results in Ref. [34] were employed to verify the modeling technique for coupling the lateral impact and axial loads.

2.2. Establishment of finite element model

The finite-element software ANSYS/LS-DYNA was used to simulate the specimens subjected to the impact load. The details of the finite element model development were presented as follows.

2.2.1. Materials model

The steel responses in numerical models were evaluated by *MAT_PIECEWISE_LINEAR_PLASTICITY model [34], which can be used to define an elasto-plastic material, and consider an arbitrary strain rate dependency. The strain rate effect on the steel was considered and the dynamic increase factor for the steel was employed by the Cowper and Symonds Model [35], as expressed in Eq. (1).

$$\mathrm{DIF} = 1 + \left(\frac{\dot{\varepsilon}}{C}\right)^{\frac{1}{p}} \tag{1}$$

where DIF is the dynamic increase factor, which means the ratio between dynamic stress and static stress; $\dot{\varepsilon}$ is strain rate; C and p were the strain rate parameters, and the values of C and p were 40.4 s^{-1} and 5, respectively [36].

The *MAT_CSCM _CONCRETE model (CSCM) was used to characterize the dynamic behavior of concrete. And it is a smooth continuous surface cap model that effectively considers the strain rate effect on the concrete, and predicts its hardening, softening and shear damage of the concrete [37]. Besides, to prevent computational difficulties with a very low stiffness, the erosion algorithm was used in this material model which was determined by the value of maximum principle strain. Referring to Ref. [38], the ERODE was set to 1.08 to accomplish element erosion. Moreover, many studies have indicated that this model can model the nonlinear response of concrete accurately under impact load [36,38,39].

The FRP material was modeled using *MAT_LAMINATED_COMPOSITE_FABRIC which is a damage mechanics-based model that can be utilized to simulate composite materials with woven fabrics complete laminates and unidirectional layers. Many studies have demonstrated that the FRP material shows a minor strain rate effect under the impact loading compared with steel and concrete [28,32,40]. The strain rate effect on FRP material was neglected in the finite element.

The *MAT_RIGID model is designed to simulate the impactor in this study, which can save the computational time and have achieved accurate results in previous studies [28,32].

2.2.2. Contact definition, boundary conditions and applying axial load

The Contact_Automatic_Surface_Surface algorithm was utilized to model the interactions between the different components. The contact algorithm can be implemented to treat contact between bodies with dissimilar material properties. In the contact algorithm, the dynamic and static friction coefficients for interface between the steel and concrete were set as 0.5 and 0.6, respectively [41]. And for the interface between impactor and FRP tube the dynamic and static friction coefficient were taken as 0.25, 0.25 for the interface between the FRP tube and concrete [28].

The keyword *Boundary_SPC_SET was used to establish the boundary conditions which were identical to the tests. The coupling of axial force and lateral impact can be divided into two phases. Phase I: The end of column was exposed to an axial force using a distributed pressure through a dynamic relaxation analysis. Phase II: The FE analysis was restarted and a lateral impact was applied to the column.

2.2.3. Hourglass type and element type

The hourglass control type 4 was introduced into the numerical model to reduce the hourglass energy effect on the simulation precision [32]. The FRP tube was simulated by the Belyschko-Tsay element. The steel, concrete and impactor were simulated using the 8-node solid hexahedron element with single point integration algorithm.

2.3. Verification of the FE model

The FEM results were shown in Fig. 1, Fig. 2 and Table 1. From Fig.1, the bending failure mode of the experimental specimens [31,34] was reasonably predicted by FE model. From Fig. 2 (a) and Fig. 2 (b), the deviations of peak impact force and plateau vale of the impact force between the predictions and test results were 5.14% and 10.07% for specimen F3L01, and were 3.15% and 3.98% for specimen F3M01. The FEM model accurately captured the trend of the impact-time history observed in experimental results. Furthermore, the maximum displacements of the FEM were lower than the experimental results, with the deviations of 13.79% and 12.93%, respectively. This can be attributed to that the slippage occurred between the clamping system and specimen [31]. Whereas, the specimens were tightly constrained in the numerical model.

From Fig.2 (c) and Fig.2 (d), the impact force-time histories of the FEM fitted the experimental results well. For specimens DBF19 and DBF20, the deviations in peak impact force between the simulations and tests were 13.91% and 4.21%, respectively. The differences in the impact plateau force between the predicted and test results were 11.22% and 3.65%, respectively. Furthermore, the deviations in the maximum displacement between the predicted and experimental results were 14.04% and 13.04% for specimens DBF19 and DBF20, respectively.

In general, the comparative analysis demonstrates that the simulation method as above can be utilized to simulate the impact responses of a GTCES column when the lateral impact and axial load are coupled.

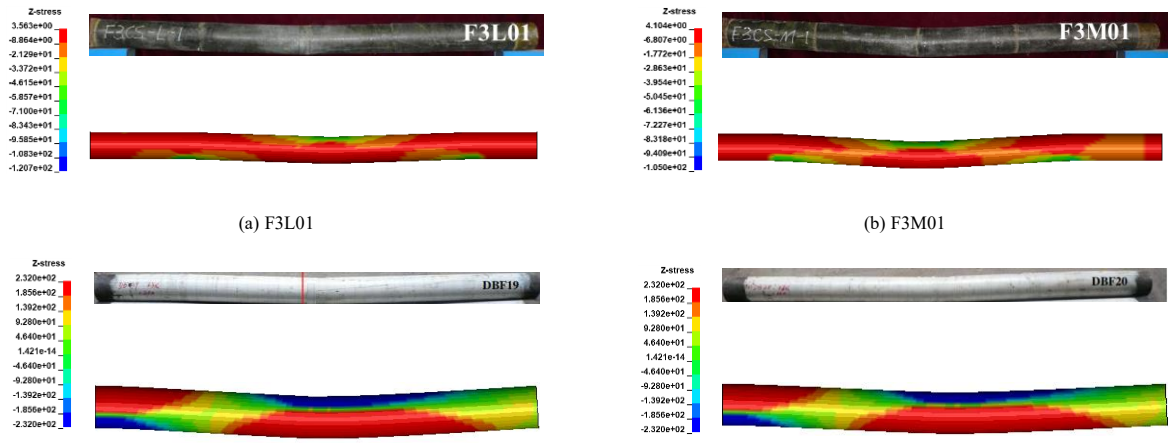

(a) F3L01 (b) F3M01

(c) DBF19 (d) DBF20

Fig. 1 Failure modes obtained from simulations and experiments

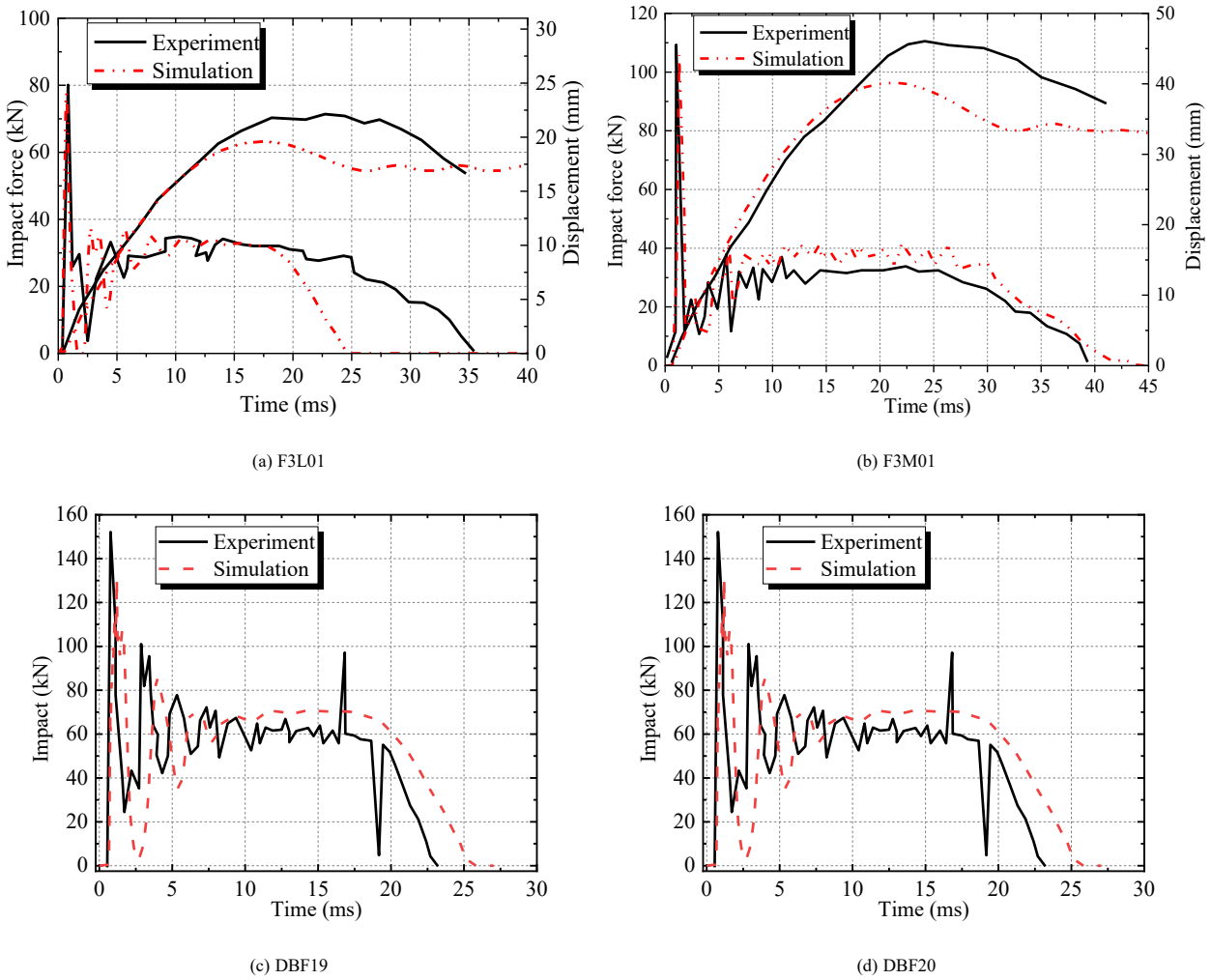

Fig. 2 Comparison of time-history curves between simulations and experiments

Table 1
Comparisons of key results [31,36]

Specimen	F_p (kN)	$F_{p,FEM}$ (kN)	Δ_{Fp}	F_{plat} (kN)	$F_{plat,FEM}$ (kN)	Δ_{plat}	δ_{max} (mm)	$\delta_{max,FEM}$ (mm)	Δ_δ
F3L01	78.8	74.7	5.14%	34.0	30.4	10.07%	23.4	19.6	13.79%
F3M01	107.8	104.4	3.15%	36.4	34.9	3.98%	47.1	40.1	12.93%
DBF19	152.1	131.5	13.91%	60.9	68.3	11.22%	17.8	20.3	14.04%
DBF20	118.1	116.3	4.21%	62.7	65.0	3.65%	25.3	28.6	13.04%

Note: F_p and $F_{p,FEM}$ are the peak impact force of test results and prediction, respectively; F_{plat} and $F_{plat,FEM}$ are the impact plateau force of test results and prediction, respectively; δ_{max} and $\delta_{max,FEM}$ are the maximum displacement of test results and prediction; Δ_{Fp}, Δ_{plat} and Δ_δ are the error of peak impact force, the impact plateau force and maximum displacement between test results and predictions, respectively.

3. FEM simulations of GTCES column

3.1. FEM modeling of GTCES column

Based on the modeling techniques described in the Section 2, a numerical simulation model of the GTCES column subjected to lateral impact was establish, as presented in Fig. 3. In this study, a 1/3 scale model of the GTCES column with a diameter of 270 mm and a height of 1300 mm and was investigated. The dimensions of the column referred to those using in office buildings [42]. The dimensions of the encased steel were plotted in Fig. 3. And the GFRP tube thickness was 5 mm, with its material properties described in Ref. [43]. The yield strength of encased steel was 235 MPa and the compressive strength of concrete was 30 MPa. The steel ratio was 3.41%, and axial force ratio was 0.3. And the calculated equations of steel ratio and axial force ratio were presented in Section 4. The axial force was applied on the column with a dynamic relaxation analysis in phase I (Fig. 3); In phase II, the freedoms of the column head were all fixed, with the stress on each component of the column were initiated using a FE analysis restarted. Finally, the impact load was applied on column.

A 10 t truck was chosen to as a vehicle model to impact the column. The vehicle mode was simplified as a flat-head impactor, which considers a rigid bumper of a truck and reduces the computational cost in simulations [38]. Referring to the [44], the heights of bumper upper and lower flanges of 10 t truck from the floor are 770 mm and 650 mm, respectively, when the truck is stationary. And the height of impact region was from 216.7 mm to 256.7 mm as considering the 1/3 scale model. Therefore, the length and width of the impactor were designed to be 280mm and 40mm as considering the diameter of the column and the width of the bumper. Referring to the scaling laws in Ref. [38], the initial kinetic energy of impactor in a small-scale model would be K^3 of those in a full-scale model and the K is the scale factor. While the velocity of the impactor is independent of scale factor K. Therefore, the impactor mass was decreased from 10 t to 0.3704 t by applying a reduction factor of 27 with a scale factor K=1/3. The impactor velocity was taken to be 10 m/s (36 km/h) in the numerical model, referring to the velocity grade of the vehicle [45].

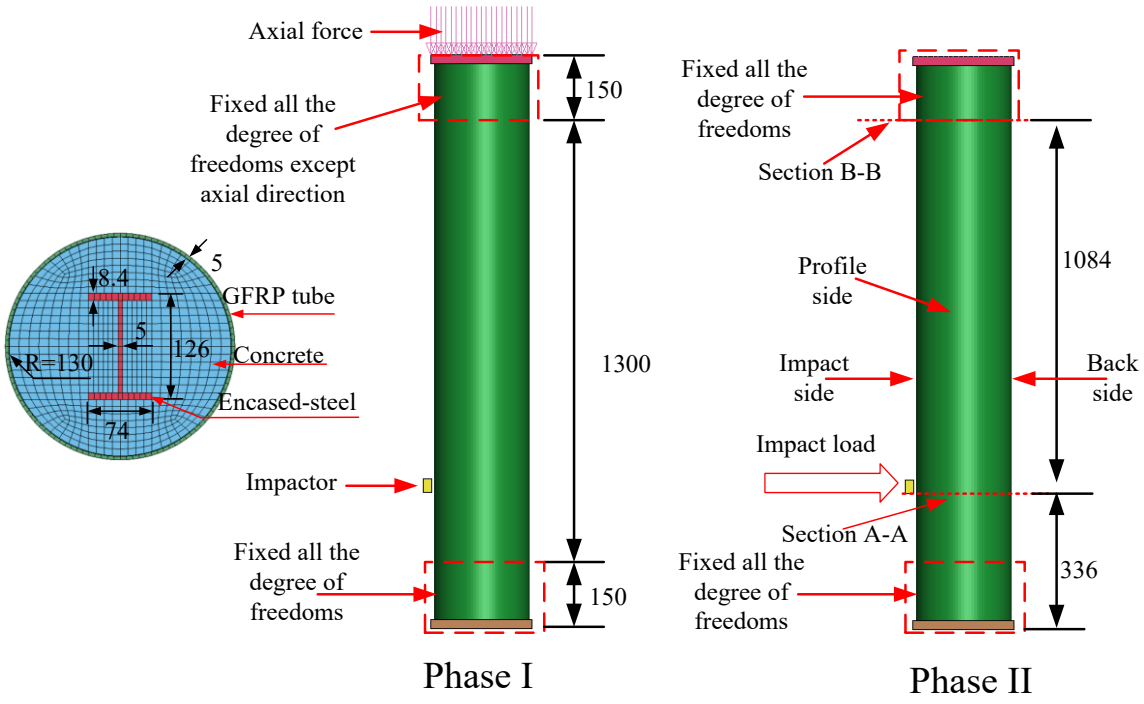

Fig. 3 Finite element model of GTCES column under lateral impact (unit/mm)

3.2. Response characteristics

3.2.1. Impact force, lateral displacement, local indication and velocity-time histories

Fig.4 showed the time-history curves of the impact force, lateral displacement (Position B), local indentation (Position A), velocity of the impactor, and velocity of the specimen. The time-histories were observed to consisted of three stages. Stage I (impact peak stage): The impactor and specimen were in contact at point O, and then the impact force rapidly increased to a peak value (1370 kN) at point A (1.409 ms); At point A, the lateral displacement was 3.98 mm, which was 30.90% of its maximum value. Additionally, the local indentation reached the maximum value 7.31 mm. Furthermore, the velocity of the specimen increased, due to the total energy transferred from impactor to the specimen as the velocity of the impactor decreased. After point A, the velocity of the specimen exceeded that of the impactor within a short period, thus indicating the specimen and impactor were separated. Which resulted in a sharp decrease in impact force until time B. Stage II (plateau stage): After point B, the velocity of specimen and impactor remained nearly constant and decreased, and underwent a small-amplitude oscillation. Additionally, the trend of impact force presents a relatively constant state. The lateral displacement gradually increased and reached its maximum value (12.88 mm) at point B (3.899 ms), indicating the ending of plateau stage. Furthermore, the impact force plateau value (F_{plateau}) was typically adopted to evaluate the impact performance of a member and was given as Eq. (1) [30,33]. The impact force plateau value of member was 844 kN.

$$F_{\text{plateau}} = \frac{\int_{t_1}^{t_2} F(t)dt}{t_2 - t_1} \tag{1}$$

where $F(t)$ was the impact force versus time curves; The t_1 and t_2 were the time points at time B and time C, respectively.

Stage III (descending stage): The velocities of the impactor and specimen were inconsistent in this stage, indicating the impactor and specimen were separated. And the specimen gradually bounced back. The impact force of the specimen decreased to zero at point D (6.719 ms). Furthermore, the residual lateral displacement and residual indentation were 10.62 mm and 4.21 mm, respectively.

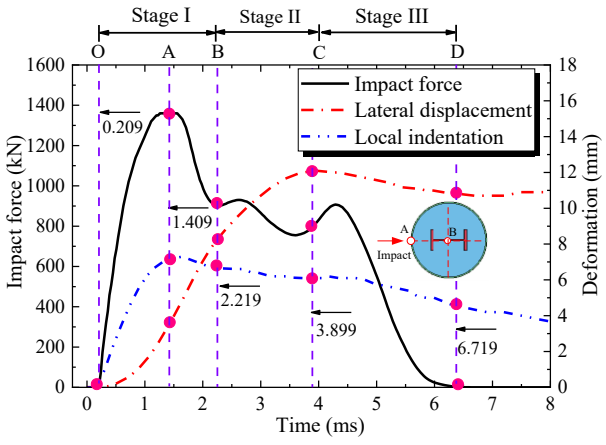

(a) Impact force, lateral displacement and local indication

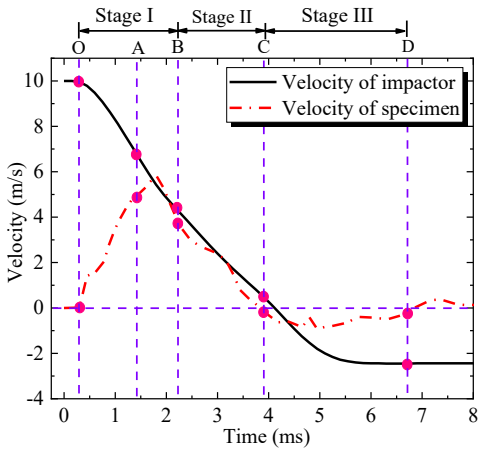

(b) Velocity of impactor and specimen

Fig. 4 Impact force, lateral displacement, local indication and velocity-time history curves

3.2.2. Shear force and bending moment along column height

The distributions of shear force and bending moment along column height were shown in Fig. 5. At 1.409 ms, the maximum shear force (-944.3 kN) and bending moment (95.8 kN·m) were observed at column height of 216 mm and 0 mm, respectively, corresponding to the lower edge of the impact area and bottom of the columns. From 1.409 ms to 3.899 ms, the maximum shear force remained at the lower edge of the impact area. With the development of impact time, the maximum shear force showed a decreasing trend. And the maximum bending moment shifted to the top of column. It demonstrated the column underwent a redistribution of the internal force. Furthermore, the highest value for bending moment showed 9.92% increment as compared to that at 1.409 ms, which was different to that of the shear force. This is because that the decrease in shear force resulted from the decrease in the impact force and the effect of inertia force. However, the lateral displacement of column gradually increased, leading to an increment in bending moment. At the end of impact, the largest shear force and bending moment appeared at the bottom of column and decreased significantly. Furthermore, a larger shear force was mainly concentrated in the area extending from the bottom column to impact area. The lager shear force area can be as a reinforcing specific region to prevent shear failure when GTCES columns subject to lateral impact.

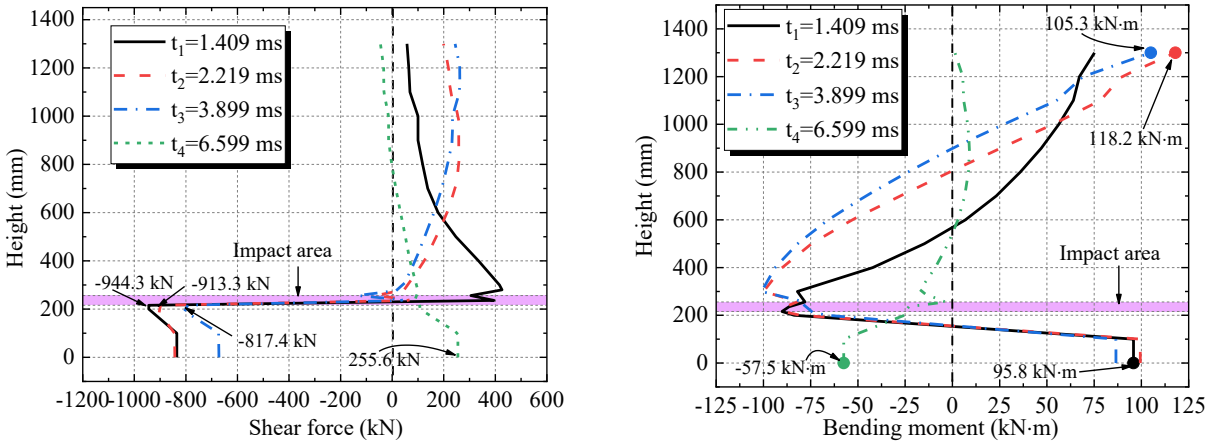

(a) Shear force (b) Bending moment

Fig. 5 Distribution of shear force and bending moment along column height

From the above discussion, the maximum shear force and bending moment occurred at the lower edge of impact area (Section A-A as shown in Fig. 3) and the top of column (Section B-B as shown in Fig. 3) during the impact, respectively. Therefore, the two sections were selected to investigate the internal force. The shear force and bending moment versus the impact time, as shown in Fig. 6. The contributions of different components to withstand shear force and bending moment were presented. From Fig. 6(a), the sign of shear force remained unchanged in the initial stage owing to that the section A-A was near the impact area. Besides, the shear force reached its maximum value (-990.3 kN) at AB stage. From Fig. 6(b), the bending moment presented negative in the initial stage, owing to the stress wave propagation. Then the bending moment gradually reached its maximum value (122.2 kN·m) at the initial of plateau stage. After the peak point, the shear force and bending moment showed downward trends. And the sign of shear force and bending moment changed at the end of descending stage due to the deformation of column recovered elastically. It can be concluded that the maximum shear force and bending moment were -990.3 kN and 122.2 kN·m and occurred at the Section A-A and Section B-B, respectively, which can provide a practical design value for dynamic shear force and bending moment.

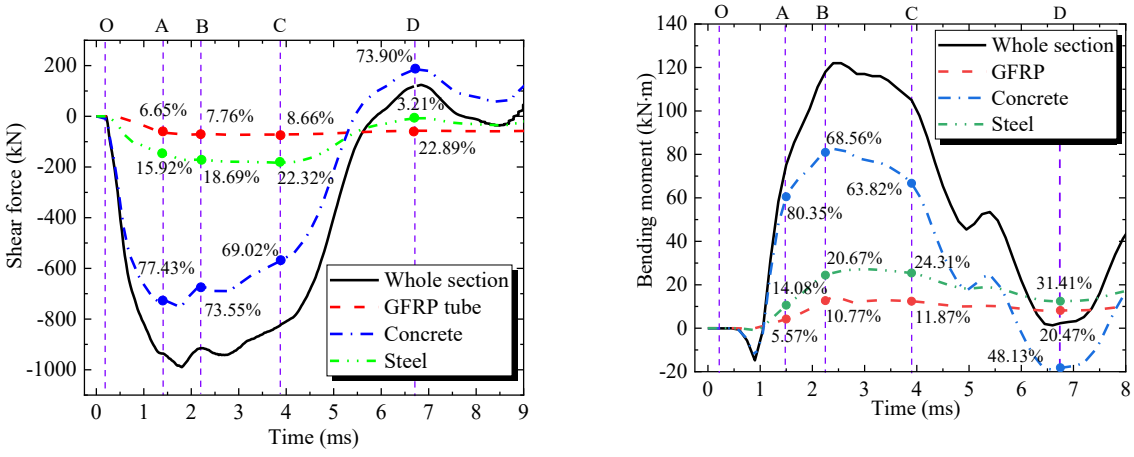

(a) Shear force at section A-A (b) Bending moment at section B-B

Fig. 6 Shear force and bending moment-time history curves

Furthermore, it can be found the shear force and bending moment were mainly withstood by the concrete, followed by the encased steel and GFRP tube. For instance, the shares of concrete in carrying the shear force and bending moment were up to 77.43% and 80.35% at A moment, respectively. During the AD stage, the share of GFRP tube and encased steel showed an increment as compared to that in OA stage. This indicated that the section underwent stress redistribution due to the concrete damage and the stress initially borne by the concrete transferred to the GFRP tube and encased steel.

3.2.3. Inertia force

When the impactor impacted the specimen, the inertia force was induced by the acceleration of specimen. The reaction and inertia force were calculated with Eq. (2), based on the force equilibrium.

$$F_{\text{impa}} + F_R + F_{\text{I}} = 0 \tag{2}$$

where F_{impa}, F_R and F_I were impact force, reaction force and inertia force, respectively.

Fig. 7 showed that the inertia and reaction force-time histories. The direction of impact force was considered to be positive. Fig. 7(a) showed that a time lag of 0.12 ms existed between the occurrence of the impact force and reaction force, indicating the response of the supports was delayed. This delay was attributed to the time required for the stress wave transfer from the impact point to supports. From Fig. 7(b), the trends of reaction and inertia forces were similar and the inertia force reached to a peak value at 0.99 ms. Furthermore, the inertia force resisted approximately 50% of the impact force in this stage. In the AC stage, the reaction force reached to a peak value in positive direction at 2.97 ms. The effect of inertia force on specimen was weaker than that during the OA stage. In the CD stage, the reaction force gradually decreased. Whereas, in the opposite direction, the inertia force increased compared to the BC stage to balance the force generated by the rebound of specimen. After the impact process, the specimen vibrated freely and the reaction force is balanced with reaction force. In summary, the influence of inertia force on GTCES column was significant in the initial and descending stages.

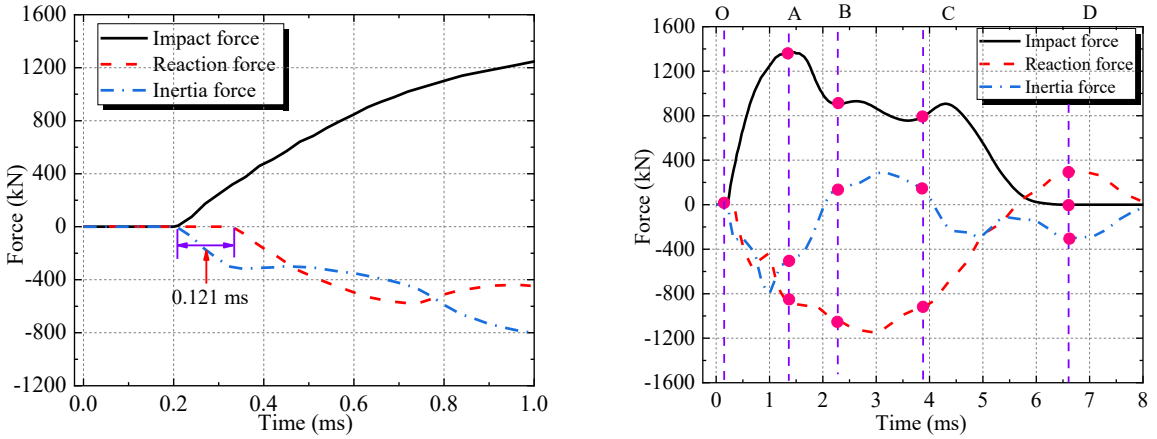

(a) Initial stage (b) Full stage

Fig. 7 Impact force, reaction force and inertia force-time histories

To investigate the influence of inertia force on the shear force and bending moment, Section A-A and Section B-B were selected. The internal shear force (F_C in Section A-A) and bending moment (M_C in Section B-B) were obtained from FEM results, and the shear force (F_F in Section A-A) and bending moment (M_F in Section B-B) induced by the impact load were calculated using Eq. (3) and Eq. (4).

$$F_F = \frac{F_{imp} \times b^2}{l^2} \tag{3}$$

$$M_F = \frac{F_{imp} \times a^2 \times b}{l^2} \tag{4}$$

where the a and b were the distance from the center of impactor to bottom and top of the column, respectively. And the l was the height of the column.

Fig. 8 plotted the F_C, F_F, F_C/F_F, M_C, M_F, and M_C/M_F time history curves. In the OA stage, the values of F_C and F_F were almost identical, and the average value of F_C/F_F was 0.99, as shown in Fig. 8(a). It suggested the inertia force had almost no influence on sectional shear force during this stage. In the AB stage, F_C/F_F increased from 1.03 to 1.52. The inertia force contributed to an increase in the sectional shear force. In the BC stage, the average F_C/F_F was 1.55 and tended to stabilize. In the CD stage, the value of F_C/F_F gradually decreased and reduced to 1.00 at 5.071 ms, demonstrating that the effect of inertia force on sectional shear force gradually decreased. From 5.071 ms to 5.882 ms, the value of F_C/F_F gradually decreased to 0, suggesting that the direction of sectional force induced by inertia force was opposite of impact load. After 5.882 ms, the value of the impact load tended to be 0 and the sectional shear force changed to opposite direction. In this stage, the sectional shear force was balanced with inertia force.

As seen in Fig. 8(b), it was possible to find that in the initial stage, the value of M_C/M_F was negative and the maximum value was -0.029, indicating bending moment due to impact load and inertia force were in opposite directions. The inertia force had a positive effect on sectional moment. After the initial stage, the sign of M_C/M_F changed and increased to 1.37 at time A. Subsequently, the value of M_C/M_F continued to increase until time B, indicating the inertia force increased the M_C. In the BC stage, the M_C/M_F tended to be consistent with an average value of 3.91. This phenomenon was similar to the inertia force effect on sectional shear force. During this stage, internal bending moment was more affected by the inertia force. In the CD stage, the value of M_C/M_F exhibited a downward trend until 4.829 ms, indicating that the effect of inertia force on sectional moment decreased. Subsequently, as the impact load decreased, the development of sectional moment was mainly driven by inertia force. Additionally, the inertia force had a greater effect on the sectional moment than the sectional shear force.

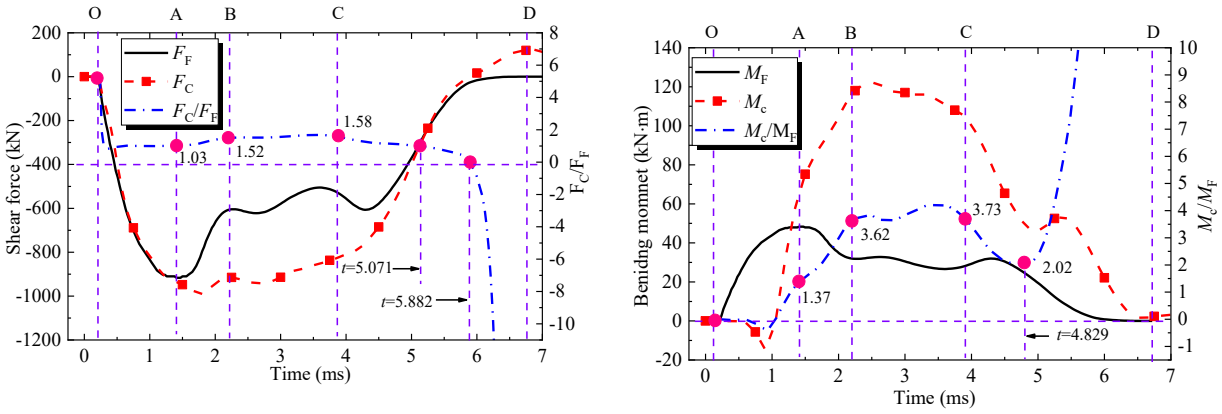

(a) F_F, F_c and F_F/F_c at section A-A (b) M_F, M_c and M_F/M_c at section B-B

Fig. 8 Effect of inertia force on shear force and bending moment

3.2.4. Energy absorption

Fig. 9 showed the energy absorption diagram of the column, which were obtained from the FEM analysis. During the OC stage, the total absorbed energy increased continuously with a decrease in the kinetic energy of impactor, reaching a maximum value at time C. Meanwhile, the kinetic energy of impactor descended to zero. This suggested the kinetic energy of impactor transferred to column continuously during this stage. After time C, the kinetic energy of impactor and total absorbed energy showed upward and downward trends, respectively. This is because the column underwent elastic recovery and the movement of the impactor reversed to the opposite direction.

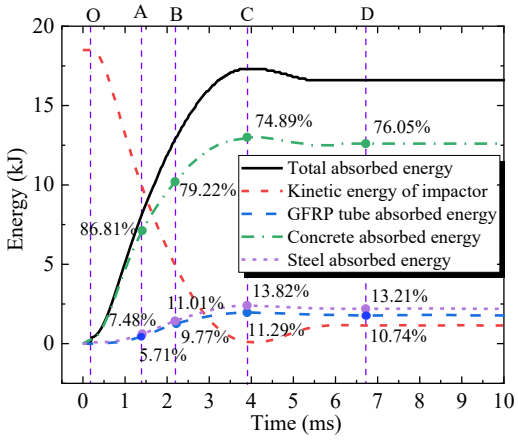

Fig. 9 Energy absorption-time history curve

Furthermore, the concrete absorbed a greater proportion of energy than other parts during the impact process. At time A, the concrete absorbed 86.81% of the energy, whereas the GFRP tube and encased steel absorbed 5.71% and 7.48%, respectively. And the concrete absorbed the higher energy owing to the local damage in impact area, which can be found in the local indentation of the column and concrete damage patterns. In addition, the total absorbed energy was 8.41kJ which was up to 48.61% of its peak value at this time, indicating that almost half of the internal energy was absorbed in this stage and the concrete in the impact area played an important role in this. In the AD stage, the concrete continued to made a significant contribution to energy absorption. Furthermore, the contribution of the encased steel and GFRP tube to absorbed energy presented an upward trend in comparison to that during the OA stage. This is because that each component of the column underwent stress redistribution as the impact developed during the AD stage.

3.2.5. Damage evolution and failure mode

The damage evolution in the column was plotted in Fig. 10. The damage to the concrete and encased steel was described by effective plastic strain. Matrix damage was used to describe damage to the GFRP tube.

At time A, the matrix damage of the GFRP tube occurred from the bottom of column to the impact area. A 45° damage path was formed between the impact side and back side. Additionally, slight damage occurred at the top of the column region on the impact side. In Section A-A, the damaged area was above 75% of the cross section. For the concrete, the cracking was initiated at the bottom of column and the impact area. The damaged area penetrated to the inner side of the flange of encased steel in Section A-A. The encased steel between the bottom of column and impact area was yielded. And the stress level on the web was higher than that on the flange. In addition, the entire cross section of the web developed into a plastic state in Section A-A. Furthermore, no damage was observed in Section B-B at time A. Subsequently, the matrix damage at the top of column and impact area propagated towards the middle of column. The more severe matrix damage to the GFRP tube was found between the bottom of the column and impact area. And the matrix damage occurred across the entire cross section in Section A-A. For the concrete, the damage level at the same location more was more severe than that at the time A. In addition, the concrete in the top zone of the column was damage on the impact side. The length of the damage zone was 19.2% of the height of the column. In Section A-A, the damaged area of the concrete increased compared to that at time A at impact side.

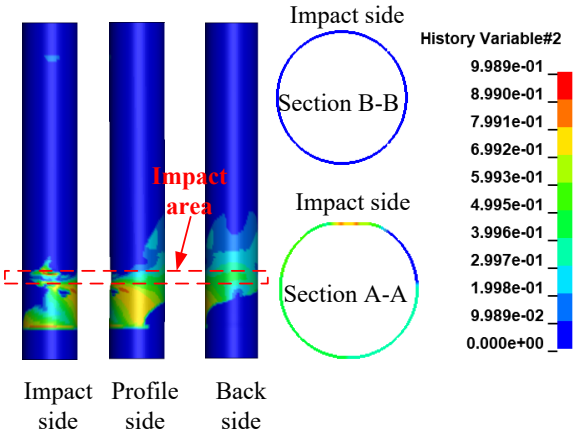

(i) GFRP tube

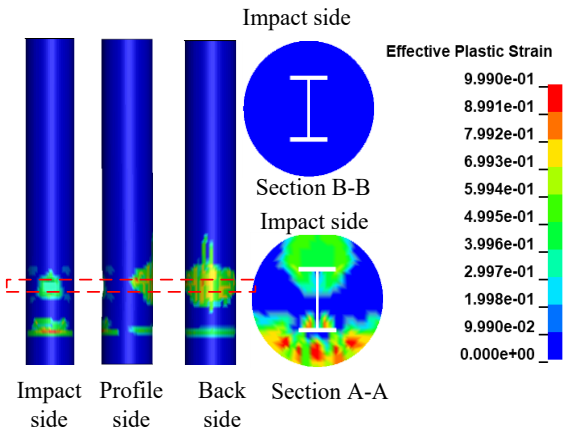

(ii) Concrete

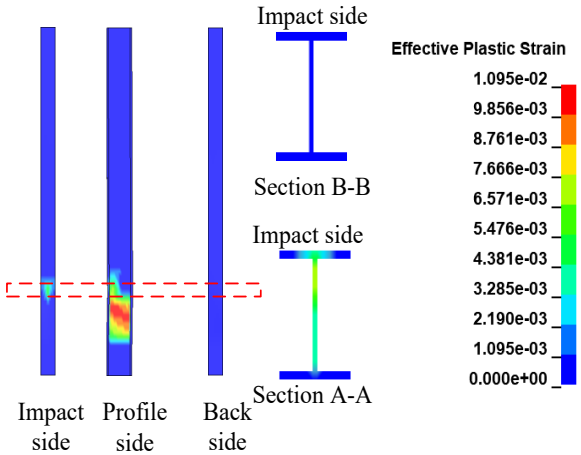

(iii) Encased steel

(a) At time A

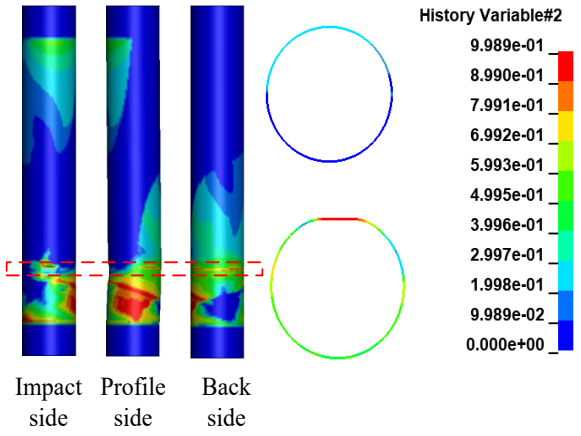

(i) GFRP tube

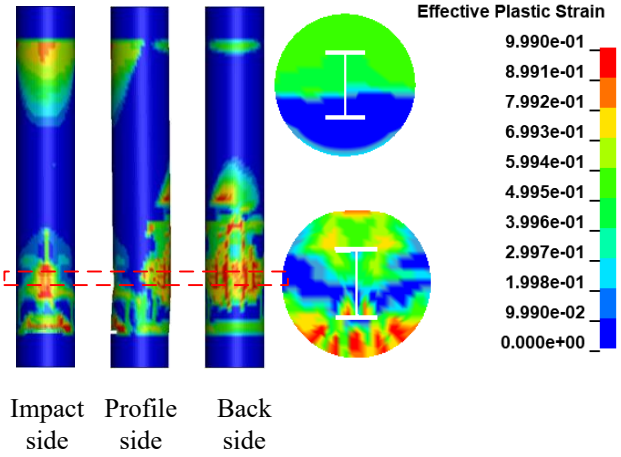

(ii) Concrete

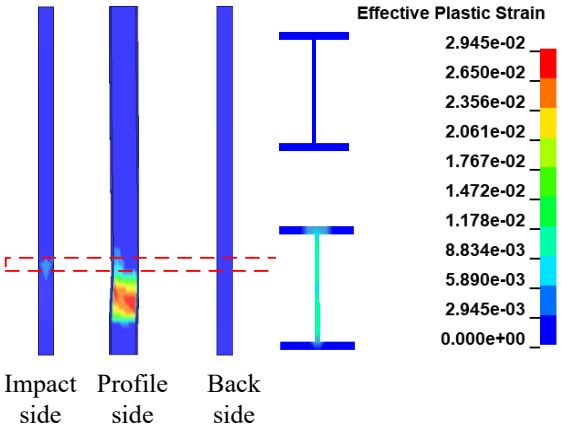

(iii) Encased steel

(b) At time B

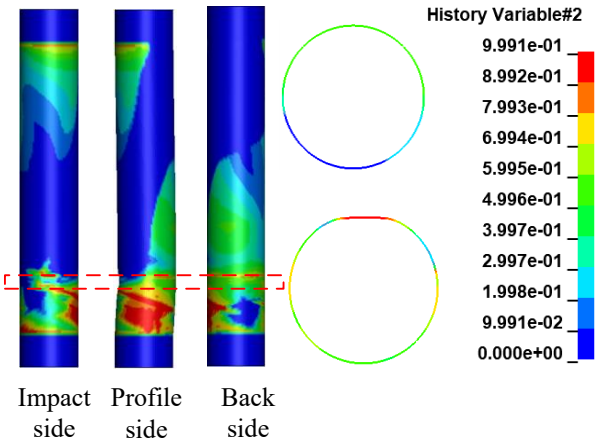

(i) GFRP tube

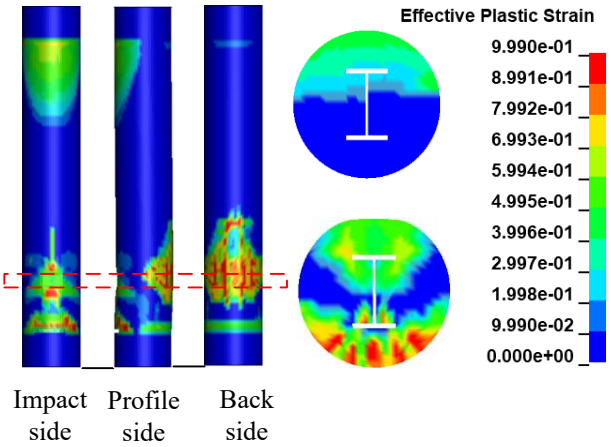

(ii) Concrete

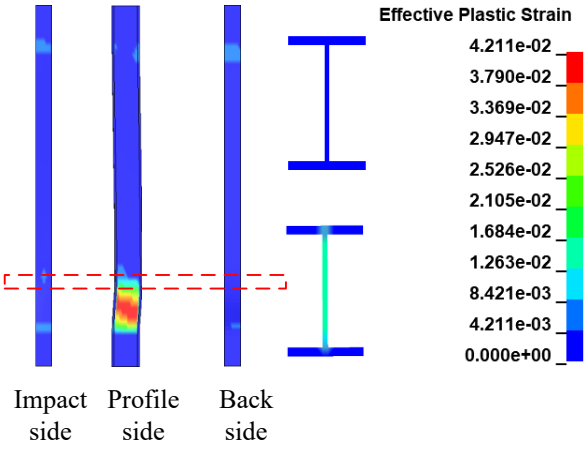

(iii) Encased steel

(c) At time C

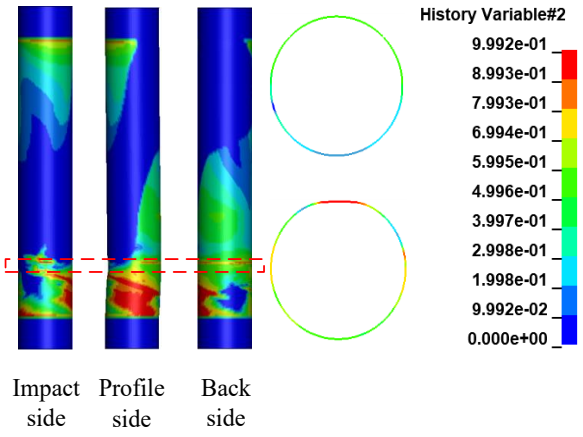

(i) GFRP tube

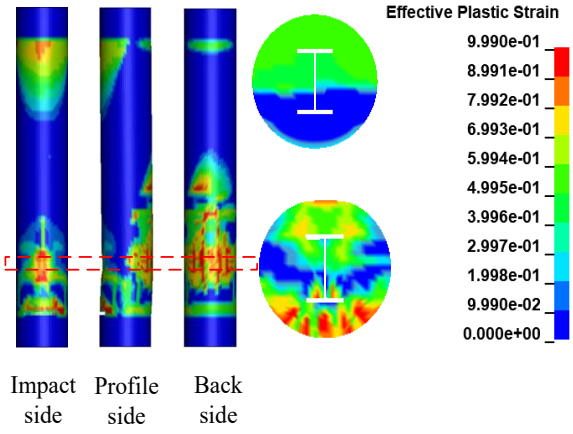

(ii) Concrete

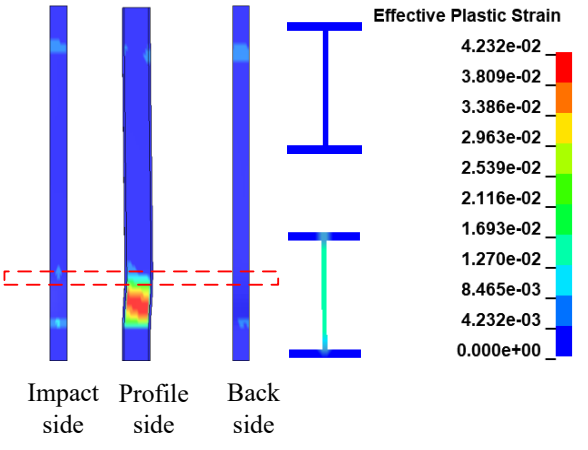

(iii) Encased steel

(d) At time D

Fig. 10 Damage evolution of the column

Furthermore, effective plastic strain area of the encased steel remained constant. Whereas, the maximum effective plastic strain value was 0.02945 which increased approximately 1.68 times compare with that at time A. Moreover, the GFRP tube and concrete at impact side presented a damage level at Section B-B. Half of the cross section was almost damage.

At time C, the matrix damage to the GFRP tube at the top of the column was severe. And the damage evolved from the impact side to back side in Section B-B. For the concrete, the damage level in the top zone increased. The damaged area had expanded to the middle of the column height. And in Section A-A and Section B-B, the damaged area increased further. Moreover, the encased steel flanges in the top and bottom zones yielded. A higher effective plastic strain area also concentrated between the bottom surface of column and impact area, and the maximum effective plastic strain was 0.04211. At time D, the concrete damage level at the contact surface between the impactor and column increased, owing to column rebound. This behavior had a minor influence on the encased steel and GFRP tube in terms of damage. Furthermore, the encased steel in Section B-B was in an elastic state during the entire impact process.

Moreover, the more severely damaged area was mainly concentrated at the

bottom of the column which was a region of higher shear force, as discussed in Section 3.2.3. And the bending moment was observed in this region. Thus, the failure model of the GTCES column under lateral impact was flexural-shear dominant.

3.2.6. GFRP tube confinement effect

The above analysis suggested that the GFRP tube made a relatively minor contribution to carrying the shear force, resisting the bending moment, and absorbing energy. However, the GFRP tube may have made a significant indirect contribution to strengthen the impact performance of column. Based on this hypothesis, a column without the GFRP tube was simulated under the identical conditions. Fig. 11 showed a comparisons of impact force and lateral displacement-time histories. The maximum impact force and plateau force of the column without a GFRP tube were 1140 kN and 655 kN, respectively. The maximum lateral displacement was 17.4 mm. The presence of GFRP tube increased the maximum impact force and plateau force by 16.78% and 22.39%, respectively. The maximum lateral displacement reduced up to 30.46%. Additionally, the column damage was shown in Fig. 12. The concrete damaged area was larger than that of column with GFRP tube. This damage was significantly more severe. And the area of the encased steel yielded remained was almost unchanged. Whereas, the maximum value of the effective plastic strain increased approximately 1.07 times compared to the column with GFRP tube. Therefore, the GFRP tube can sustain a higher impact force on the column, because the GFRP tube confined the concrete, which indirectly improved the column's dynamic resistance. The circular stress of GFRP tube under impact was presented in Fig. 13, and was used to investigate the confinement effect that benefited from GFRP tube. The GFRP tube was almost in a tensile state along the hoop direction, except for a few areas at the bottom and top of column. It indicated that the GFRP tube can effectively provide concrete confinement. Compared with the column without a GFRP tube, the confinement effect reduced the concrete damage level. The location of the more severe concrete damage in the column without a GFRP tube coincided with areas where the GFRP tube in the GTCES column provided higher confinement effect. Furthermore, the circular stress of the GFRP tube was higher in the impact region during the plateau stage (Fig. 13 (b) and Fig. 13(c)). It would provide the excellent confinement effect for concrete, thus preventing the concrete damage and reducing the deformation of encased steel, resulting in higher plateau force and lower lateral displacement.

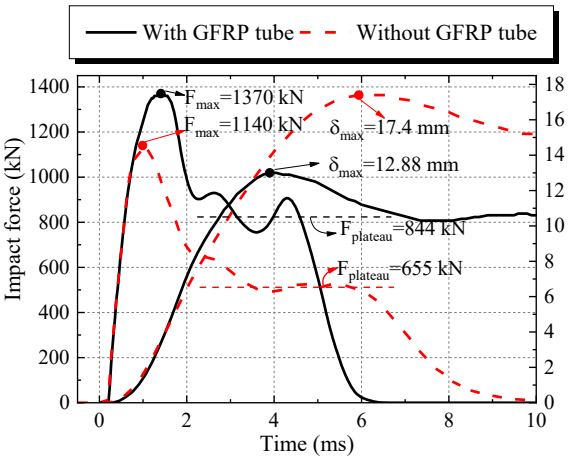

Fig. 11 Impact force and lateral displacement-time histories of the column without GFRP tube

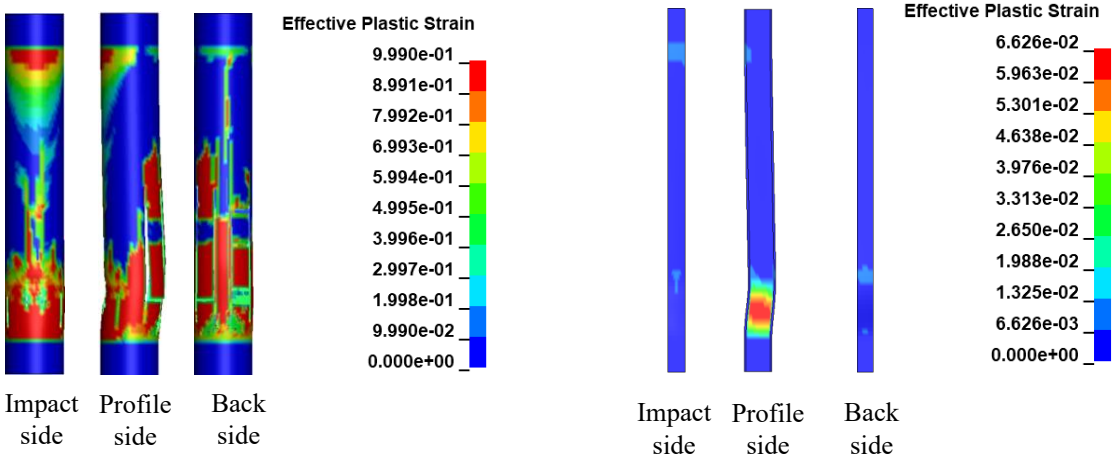

(a) Concrete (b) Encased steel

Fig. 12 Failure modes of the column without GFRP tube

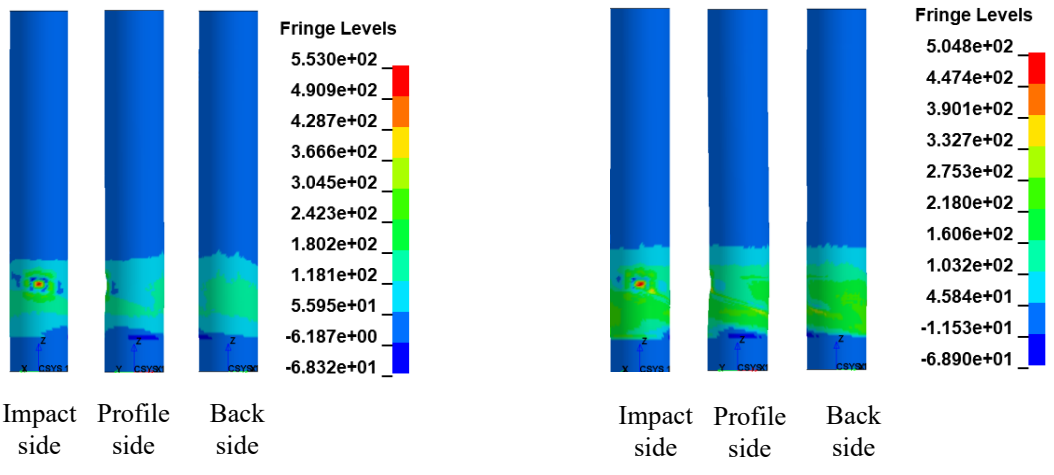

(a) At time A (b) At time B

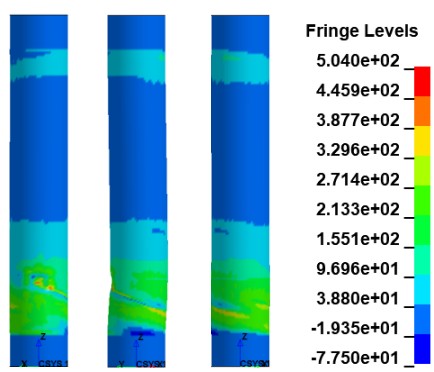

(c) At time C

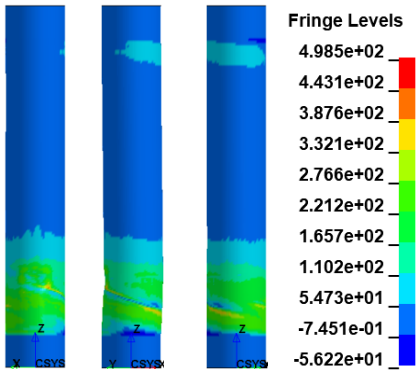

(d) At time D

Fig. 13 Stress of the GFRP tube along the circular direction

Table 2
The results of parametric analysis

Group	n	f_c(MPa)	f_y(MPa)	α	v (m/s)	F_p (kN)	F_{plat} (kN)	Δ_{1max} (mm)	Δ_{1resi} (mm)	Δ_{2max} (mm)	Δ_{2resi} (mm)
Axial force ratio	0	30	235	3.41%	10	1180	801	13.81	10.62	8.69	5.12
	0.15	30	235	3.41%	10	1310	802	13.32	10.62	7.61	4.23
	0.3	30	235	3.41%	10	1370	844	12.88	10.31	7.31	4.21
	0.45	30	235	3.41%	10	1400	854	12.63	10.25	7.18	4.22
	0.6	30	235	3.41%	10	1410	868	12.51	10.21	6.71	4.20
Concrete strength	0.3	30	235	3.41%	10	1370	844	12.88	10.62	7.31	4.21
	0.3	40	235	3.41%	10	1520	927	11.52	9.07	6.59	2.83
	0.3	50	235	3.41%	10	1590	998	10.71	8.08	6.81	3.12
Encased Steel yield strength	0.3	30	235	3.41%	10	1370	844	12.88	10.31	7.31	4.21
	0.3	30	355	3.41%	10	1410	874	12.31	9.82	7.33	4.18
	0.3	30	390	3.41%	10	1430	887	12.02	9.41	7.39	4.19
	0.3	30	420	3.41%	10	1440	899	11.83	9.23	7.23	3.57
Steel ratio	0.3	30	235	3.41%	10	1370	844	12.88	10.31	7.31	4.21
	0.3	30	235	4.92%	10	1450	932	11.51	9.67	7.22	4.19
	0.3	30	235	6.69%	10	1630	1129	8.58	6.45	6.68	4.15
Impact velocity	0.3	30	235	3.41%	10	1370	844	12.88	10.31	7.31	4.21
	0.3	30	235	3.41%	15	1700	836	27.81	24.83	11.31	6.71
	0.3	30	235	3.41%	20	2030	797	55.72	51.03	11.32	7.32
	0.3	30	235	3.41%	25	2280	787	85.83	79.91	15.61	7.31

Note: n was the axial force ratio; f_c was the compressive strength of concrete; f_y was the encased steel yield strength; α was the steel ratio; v was the impact velocity; F_p and F_{plat} were the impact force and impact force plateau value, respectively; Δ_{1max} and Δ_{1resi} were peak and residual lateral displacement; Δ_{2max} and Δ_{2resi} were peak and residual local indentation.

4. Parametric analysis

The impact response of GTCES column for different influence parameters were analyzed in this section. The parameters included the axial force ratio, concrete strength, encased steel yield strength, steel ratio and impact velocity. The results were listed in Table 2.

4.1. Axial force ratio

Five axial force ratios (0, 0.15, 0.3, 0.45, 0.6) were selected to explore the effects of axial force ratio on GTCES column under impact. The axial force ratio was calculated by:

$$n = \frac{N_0}{N_u} \tag{5}$$

where N_0 is the applied axial force and N_u is the ultimate axial force of the column, which was determined as described previously [46].

Fig. 14(a) showed the impact force-time histories and impact force values under different axial force ratios. The impact force-time histories exhibited the same trend. With increasing of axial force ratio, the peak and plateau impact force increased. When the axial force ratio ranged from 0 to 0.6, the peak impact force increased by 11.01%, 16.10%, 18.64% and 19.49%, indicating that applying the axial force enhanced the local stiffness of the impact area. The increase in plateau force was slight, and corresponding increases of 0.21%, 5.34%, 6.67% and 8.33% were observed. Meanwhile, the increase in impact force values was small when the axial force ratio exceeded 0.3.

Fig. 14(b) showed that the lateral displacement-time history curves under different axial force ratios. The changing trends of displacement-time histories under different axial force ratios were almost identical. Both the peak and residual lateral displacements exhibited downward trends by increasing the axial force ratio. The peak lateral displacements were reduced by 3.62%, 5.79%, 8.69% and 9.42%, the residual lateral displacement decreased by 2.75%, 5.51%, 5.96% and 6.42%, when the axial force ratio increased from 0 to 0.15, 0.3, 0.45 and

0.6, respectively. Furthermore, Fig. 14(c) showed the local indentation-time histories under different axial load ratios. The peak local indentation decreased by 12.54%, 15.60%, 17.38% and 22.78%, respectively, with increasing axial force ratio. The residual local indentation remained relatively unchanged as the axial force ratio exceeded 0.

The damage of column (n=0) at times A and C was presented in Fig. 15. At time A, the damage level of each component in the impact area was severe than that of the column (n=0.3), as presented in Fig. 15(a). This suggested that increasing the axial force ratio enhanced the local stiffness of the impact area, thereby contributing to an increase in the peak impact force. At the time C, the column (n=0) damage level was much more severe in comparison to that of the column (n=0.3), as presented in Fig. 10(d), indicating a higher axial force ratio can reduce the damage level of the column during plateau stage, thereby leading to higher impact performance. This was owing to that the stiffness of the column can be improved by increasing the axial force ratio.

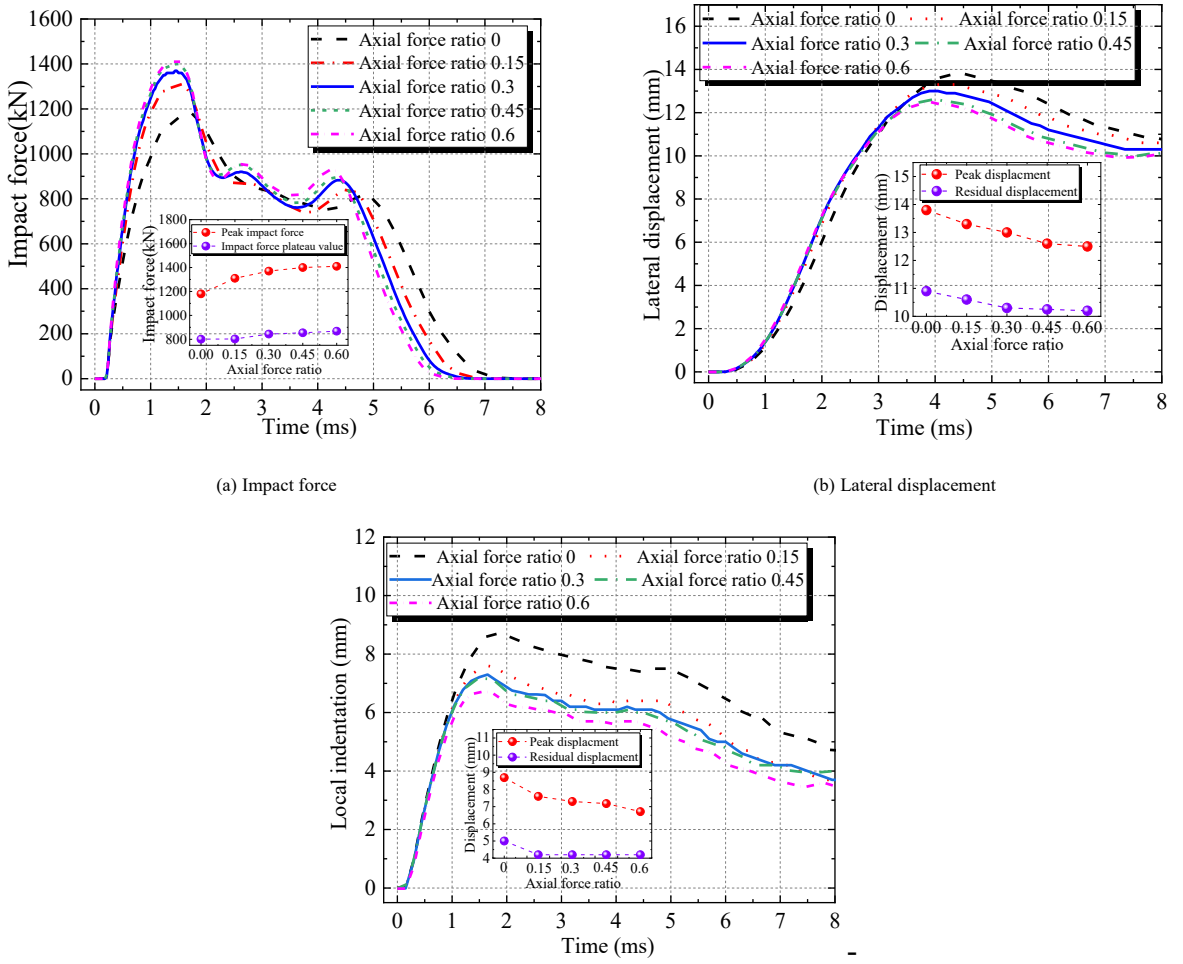

(a) Impact force

(b) Lateral displacement

(c) Local indentation

Fig. 14 Impact force, lateral displacement and local indentation-time history curves under different axial forces

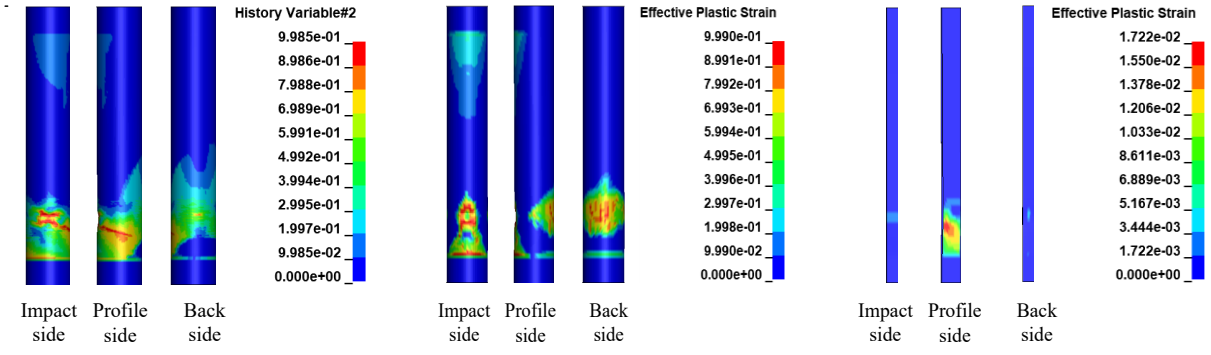

(a) GFRP tube

(b) Concrete

(c) Encased steel

(a) At time A

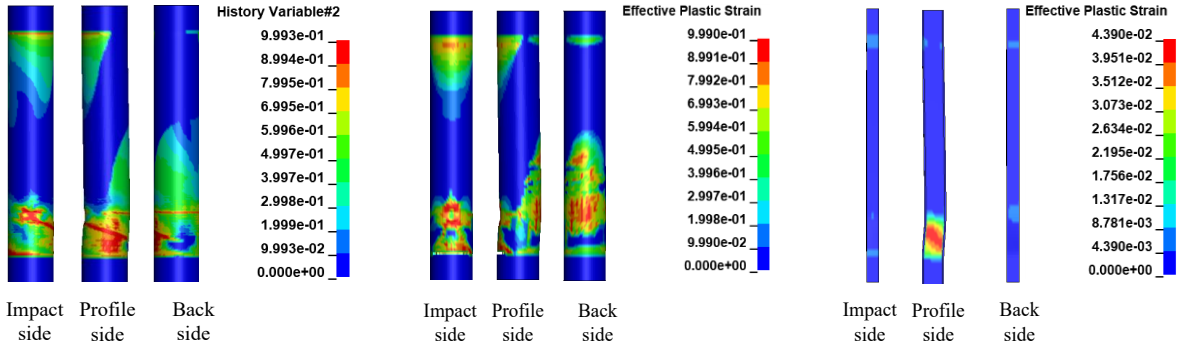

(d) GFRP tube (e) Concrete (f) Encased steel

(b) At time B

Fig. 15 Damage evolution of the column (n=0)

4.2. Concrete strength

The effects of three different concrete strengths (30MPa, 40MPa, and 50MPa) on the impact characteristics of the GTCES columns were explored. Table 2 and Fig. 16 showed the numerical simulation results. Fig. 16(a) illustrated that the concrete strength significantly affected on impact force. As the concrete strength increasing from 30MPa to 40MPa and 50MPa, the peak impact force increased by 10.95% and 16.06%, and led to an enhancement of 9.83% and 18.25% for impact force plateau value, respectively. This phenomenon differed from that observed in previous study [32]. Fig. 16(b) showed that the peak and residual lateral displacements could be reduced by increasing the concrete strength. The peak lateral displacements decreased to 10.56% and 16.84%, and the decreases of residual lateral displacements were 14.59% and 23.91%, respectively. Meanwhile, Fig. 16(c) showed that increasing the concrete strength can reduce local indentation. The peak local indentation was reduced by 9.84% and 6.84%, and the residual local indentation was reduced by 32.77% and 25.89%, respectively. Increasing the concrete strength is a useful approach to improve the dynamic performance of the GTCES.

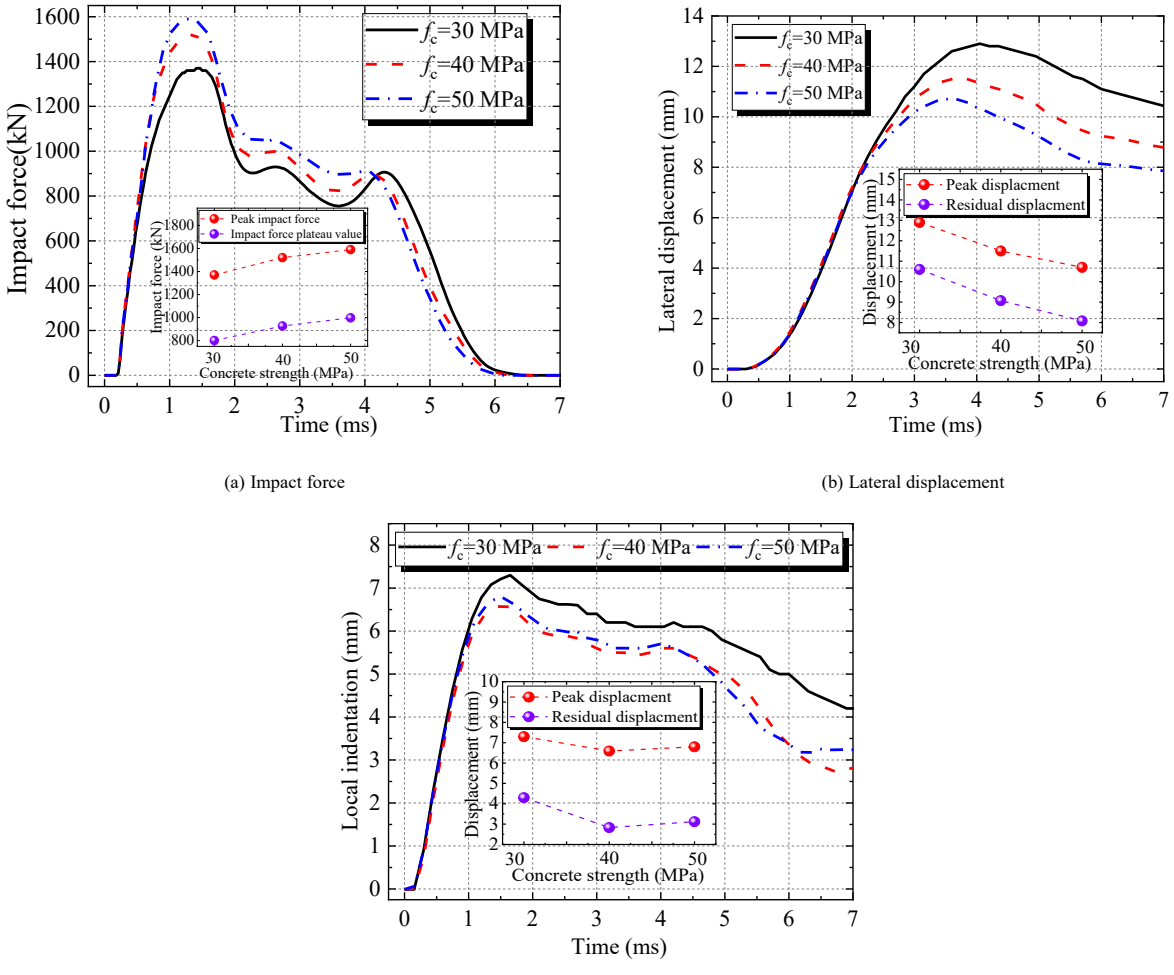

(a) Impact force (b) Lateral displacement

(c) Local indentation

Fig. 16 Impact force, lateral displacement and local indentation time history curves under different concrete strengths

4.3. Encased steel yield strength

Fig. 17 and Table 2 presented the dynamic responses of the GTCES with various encased yield strengths (235MPa, 355MPa, 390MPa and 420MPa). The findings indicated the peak impact force increased by 2.92%, 4.38% and 5.11%, and the plateau force increased by 3.55%, 5.09% and 6.52%, by increasing the encased steel yield strength from 235 MPa to 355 MPa, 390 MPa and 420 MPa, respectively. Which indicated that increasing the yield strength of the encased steel had a slight influence on the impact force value. The reason for this was that the contribution of encased steel to impact resistance was lower.

Fig. 17(b) showed that the lateral displacement-time histories and its characteristic displacement values under different steel strengths. The peak and residual lateral displacements were slightly decreased by increasing the yield strength of encased steel. When the encased steel yield strength increased from 235 MPa to 355 MPa, 390 MPa and 420 MPa, the peak lateral displacement decreased by 3.91%, 6.25% and 7.81%, and the residual lateral displacement decreased by 7.53%, 11.39% and 13.09%, respectively. From Fig. 10(c) and Fig. 18, as the encased steel yield strength increased, the effective plastic strain of the encased steel correspondingly decreased. This demonstrated that increasing the encased steel yield strength would produce less plastic deformation and more elastic deformation, thereby reducing the residual lateral displacement. From Fig. 17(c), the encased steel yield strength had a minor influence on the local indentation. This was because that the local indentation was induced by concrete deformation.

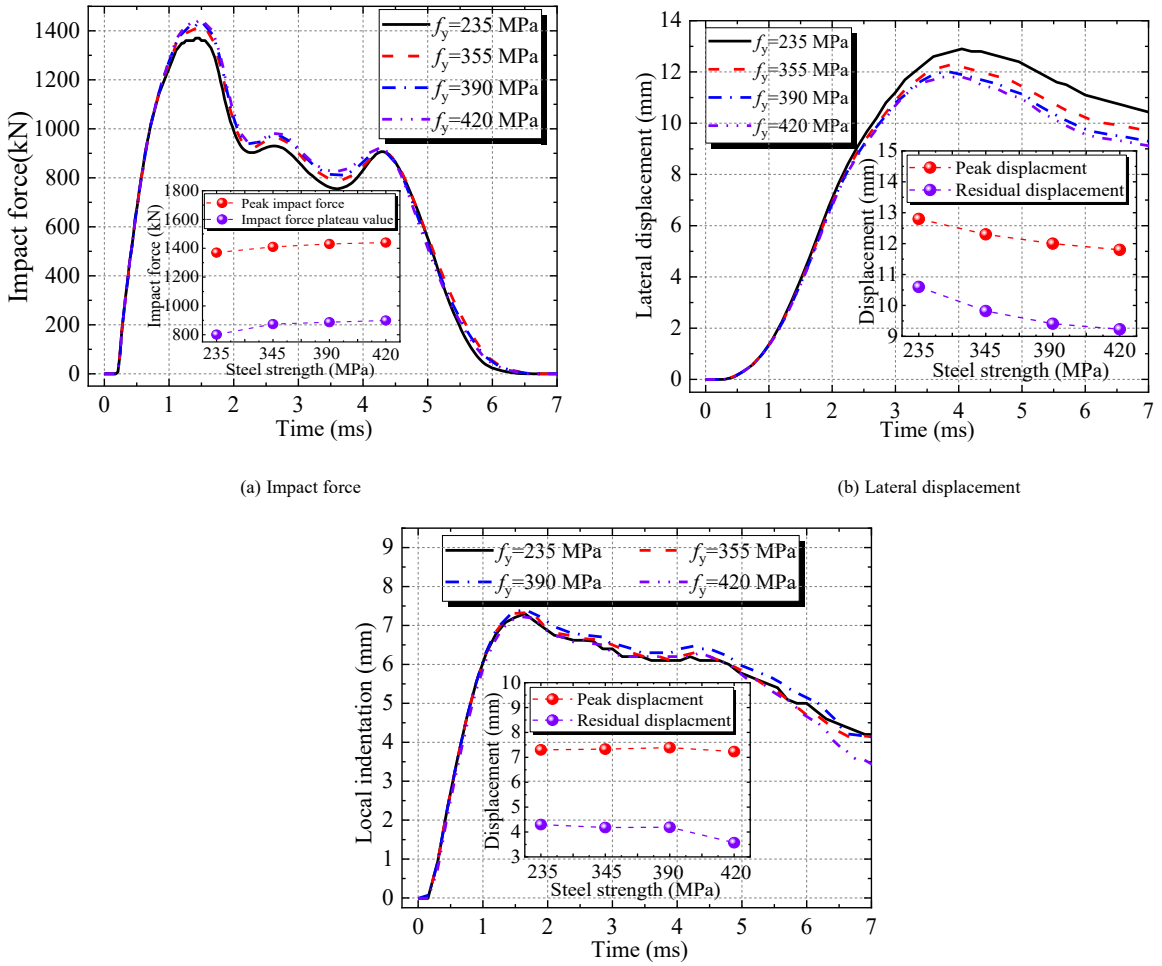

(a) Impact force

(b) Lateral displacement

(c) Local indentation

Fig. 17 Impact force, lateral displacement and local indentation time history curves under different encased steel yield strengths

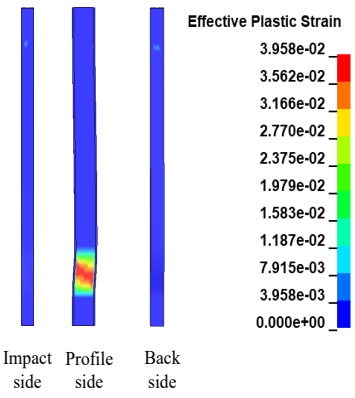

Fig. 18 Effective plastic strain of the encased steel at time C (420 MPa)

4.4. Steel ratio

The simulation results for the GTCES with varying the steel ratios (3.41%, 4.92% and 6.69%) were shown in Fig. 19. The steel ratio was determined according to the method described in Ref. [22], with the actual dimensions of the encased steel considered [47].

Fig. 19(a) illustrated that when the steel ratio increased from 3.41% to 4.92% and 6.69%, the peak impact force increased by 5.84% and 18.98%, respectively. This suggested that the local stiffness of the impact area was enhanced by an increase in steel ratio. Meanwhile, the enhancements in the impact force plateau values were 10.42% and 33.77%, respectively. The steel ratio had a greater effect on the impact force plateau value than on the peak impact force. This was because that encased steel played a greater role in absorbing energy and bearing the load in the plateau stage than in the initial stage, as discussed in Section 3.

Furthermore, Fig. 19(b) illustrated that the lateral displacement decreased as the steel ratio increased. The reductions in the peak lateral displacement were 10.63% and 33.39%, while the reductions in the residual lateral displacement were 8.95% and 39.27%, via increasing the steel ratio from 3.41% to 4.92% and 6.69%. This was because that the sectional bending stiffness of the column was enhanced by increasing the steel ratio. Whereas, the steel ratio contributed slightly to reduction in local indentation, as shown in Fig. 19(c).

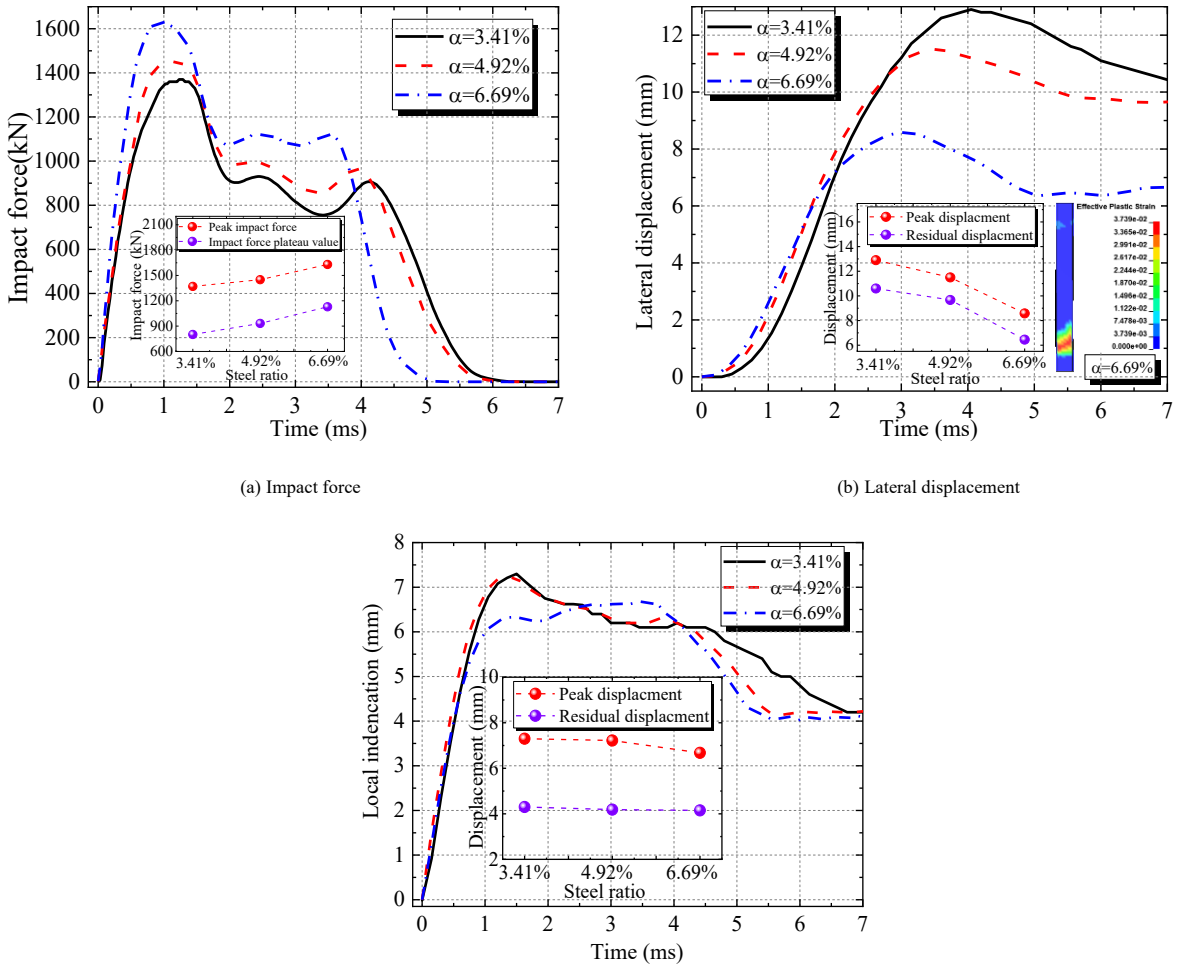

(a) Impact force

(b) Lateral displacement

(c) Local indentation

Fig. 19 Impact force, lateral displacement and local indentation time history curves under different steel ratios

4.5. Impact velocity

Four different impact velocities were considered to explore the impact performance of GTCES column. Fig. 20 exhibited a comparison of the GTCES with varying impact velocities. From Fig. 20 (a), when the impact velocity increased from 10 m/s to 15 m/s, 20 m/s and 25 m/s, the enhancements of the peak impact force were 24.09%, 48.18% and 66.42%, respectively. It suggested that the local dynamic response increased under a higher impact velocity. Nevertheless, Fig. 21 showed that the more severe damage occurred on the column in the initial stage. This was because a higher proportion of impact energy was absorbed in this stage.

Increasing the impact velocity reduced the impact resistance. The impact force plateau value showed a minor reduction (6.75%), as the impact velocity increased from 10 m/s to 25 m/s. However, this reduction level was not significant. A possible reason was that the strength of encased steel and concrete was improved owing to the strain rate effect under a higher impact velocity, thereby improving their ability to resist the impact load.

From Fig. 20(b), the increases in the lateral peak displacement were 1.16 times, 3.33 times and 5.66 times, and the increases in the lateral residual displacement were 1.34 times, 3.81 times and 6.54 times, via increasing impact velocity from 10m/s to 15 m/s, 20 m/s and 25 m/s, respectively. And the increases in the peak and residual lateral displacements were significant. This was because of the severe damage that occurred in the column during the initial stage under a higher impact velocity, which significantly reduced the stiffness of the column. In addition, a greater proportion of the impact energy was absorbed during the plateau stage, resulting in a more significant deformation of the column to absorbed impact energy.

Fig. 20(c) showed that the increases in the local peak indentation were 54.79%, 55.86% and 1.13 times, respectively, and the increases in the local residual indentation were 55.81%, 69.76% and 70.02%, respectively. It was evident that the local damage in the impact area was more severe under higher impact velocity. Furthermore, the increase in the local indentation was lower than that in the lateral displacement. This illustrated that the lateral deformation of column contributed significantly to absorb impact energy.

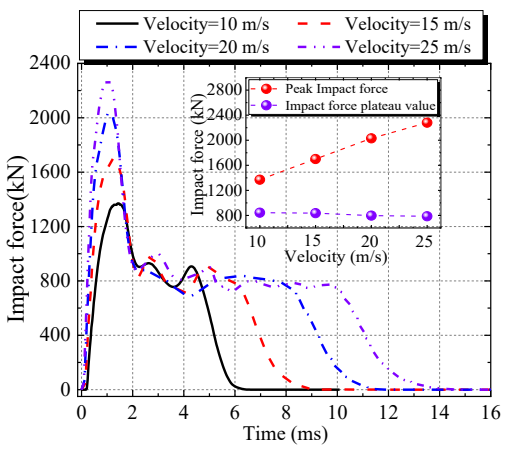

(a) Impact force-time history

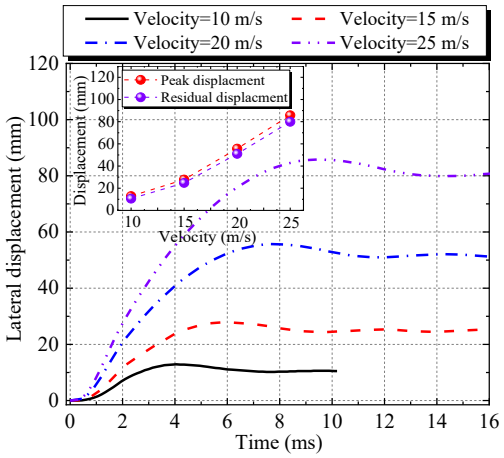

(b) Lateral displacement-time history

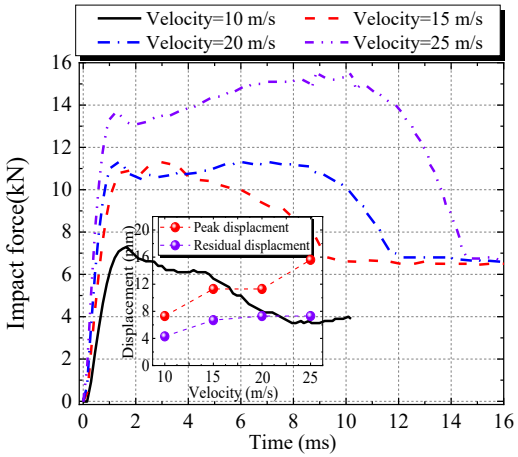

(c) Local indentation-time history curve

Fig. 20 Impact force, lateral displacement and local indentation time-history curves under different impact velocities

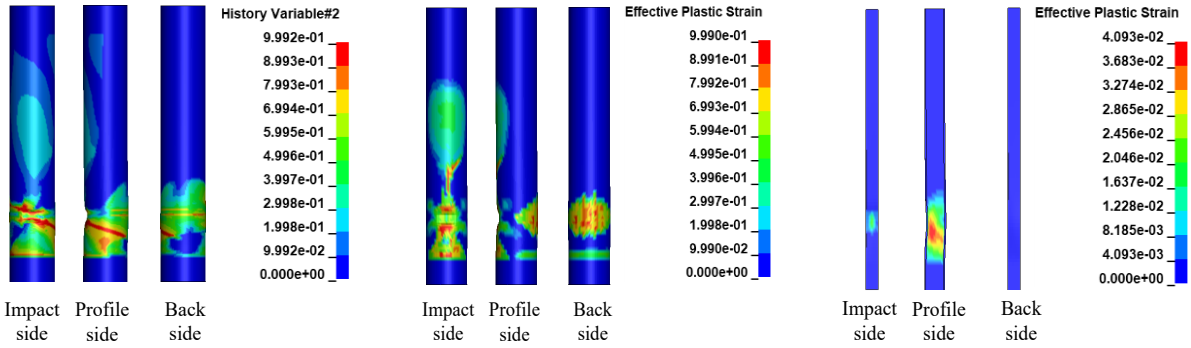

(a) GFRP tube (b) Concrete (c) Encased steel

(a) At time A

Fig. 21 Damage evolution of the column under the impact velocity of 25m/s (at time A)

5. Conclusions

The dynamic behaviors of the GTCES column with fixed ends under lateral impact load were investigated using a finite element technique in this study. According to these findings, it can be concluded as:

(1) The inertial and reaction force combine to resist the impact, with the inertial force resisting approximately 50% of the impact force during the impact peak stage. The inertia force increases the sectional bending moment and shear force.

(2) Before the unloading stage, the proportions of the bending moment, shear force and energy absorption borne by the concrete are significant and can reach over 63%, 75% and 74%, respectively. The GFRP tube as a confinement system for the concrete can significantly reduce the damage to the column, which indirectly enhances the impact performances of the GTCES column.

(3) More severe damage concentrates in the area from the bottom of the column to the impact region, which is a region of higher shear. The lager shear force area can be as a reinforcing specific region to prevent shear failure. The failure model of GTCES column was flexural-shear dominant.

(4) Increasing the axial force ratio can enhance the local stiffness of the column, the peak local indentation decreases by 22.78% and the peak impact force increases by 19.49%, respectively, with increasing the axial force ratio from 0 to 0.6. A higher impact velocity will induce more severe damage in the impact peak stage, thus the impact resistance of the column is reduced significantly.

(5) The steel ratio significantly affects the impact resistance of the column, followed by the concrete strength and encased steel yield strength. Additionally,

increasing the concrete strength can effectively reduce the peak and residual local indentations.

Data availability

All data, models, and code generated or used in this study appear in the submitted article.

Funding

This work was supported by the National Natural Science Foundation of China (grant number 52278196); Key Projects of National Natural Science Foundation of China (grant number 51938009).

Declaration of conflicting interests

The authors declared that there are no conflicts of interest.

References

[1] L. Huang, S.S. Zhang, T. Yu, Z.Y. Wang, Compressive behaviour of large rupture strain FRP-confined concrete-encased steel columns, Constr. Build. Mater. 183 (2018) 513-522, http://dx.doi.org/10.1016/j.conbuildmat.2018.06.074.

[2] L. Huang, P. Yin, L. Yan, B. Kasal, Behavior of hybrid GFRP-perforated-steel tube-encased concrete column under uniaxial compression, Compos. Struct. 142 (2016) 313-324, http://dx.doi.org/10.1016/j.compstruct.2016.02.016.

[3] K. Karimi, W.W. El-Dakhakhni, M.J. Tait, Performance enhancement of steel columns using concrete-filled composite jackets, J. Perform. Constr. Facli. 25 (2011) 189-201, http://dx.doi.org/10.1061/(ASCE)CF.1943-5509.0000162.

[4] T. Yu, J.G. Teng, Y.L. Wong, Stress-strain behavior of concrete in hybrid FRP-concrete-steel double-skin tubular columns, J. Struct. Eng. 136 (2010) 379-89, http://dx.doi.org/10.1061/ASCEST.1943-541X.0000121.

[5] T. Yu, Y.L. Wong, J.G. Teng, Behavior of hybrid FRP-concrete-steel double-skin tubular columns subjected to eccentric compression, Adv. Struct. Eng. 13 (2010) 961-74, http://dx.doi.org/10.1260/1369-4332.13.5.961.

[6] T. Yu, J.G Teng, Behavior of hybrid FRP-concrete-steel double-skin tubular columns with a square outer tube and a circular inner tube subjected to axial compression, J. Compos. Constr. 17 (2013) 271-9, http://dx.doi.org/10.1061/(ASCE)CC.1943-5614.0000331

[7] T. Ozbakkaloglu, Y. Idris, Seismic behavior of FRP-high-strength concrete-steel double-skin tubular columns, J. Struct. Eng. 140 (2014) 04014019, http://dx.doi.org/10.1061/(ASCE)ST.1943-541X.0000981.

[8] B. Zhang, T.G. Teng, T. Yu, Experimental behavior of hybrid FRP-concrete-steel double-skin tubular columns under combined axial compression and cyclic lateral loading, Eng. Struct. 99 (2015) 214-31, http://dx.doi.org/10.1016/j.engstruct. 2015.05.002.

[9] Xiao, Applications of FRP composites in concrete columns, Adv. Struct. Eng. 7 (2004) 335-43, http://dx.doi.org/10.1260/1369433041653552.

[10] Y.M. Hu ,T. Yu, J.G. Teng, FRP-confined circular concrete-filled thin steel tubes under axial compression, J. Compos. Constr. 15 (2011) 850-60, http://dx.doi.org/10.1061/(ASCE)CC.1943-5614.0000217.

[11] J.G. Teng, Y.M. Hu, T. Yu, Stress-strain model for concrete in FRP-confined steel tubular columns, Eng. Struct. 49 (2013) 156-67, http://dx.doi.org/10.1061/ASCEST.1943-541X.0000121.

[12] T. Yu, Y. Hu, J.G Teng, FRP-confined circular concrete-filled steel tubular columns under cyclic axial compression, J. Constr. Steel. Res. 94 (2014) 33-48, http://dx.doi.org/10.1061/10.1016/j.jcsr.2013.11.003.

[13] A. Mirmiran, M. Shahawy, Behavior of concrete columns confined by fiber composites, J. Struct. Eng. 123 (5) (1997) 583-590, http://dx.doi.org/10.1061/(asce)0733-9445(1997)123:5(583).

[14] T. Jiang, J.G. Teng, Analysis-oriented stress-strain models for FRP-confined concrete, Eng. Struct. 29 (11) (2007) 2968-2986, http://dx.doi.org/10.1016/j.engstruct.2007.01.010.

[15] T. Yu, G. Lin, S.S. Zhang, Compressive behavior of FRP-confined concrete-encased steel columns, Compos. Struct. 154 (2016) 493-506, http://dx.doi.org/10.1016/j.compstruct.2016.07.027.

[16] X. Liu, A. Nanni, P.F. Silva, Rehabilitation of compression steel members using FRP pipes filled with non-expansive and expansive light-weight concrete, Adv. Struct. Eng. 8 (2) (2005) 129–42, http://dx.doi.org/10.1260/1369433054038029.

[17] K. Karimi, M.J. Tait, W.W. El-Dakhakhni, Testing and modeling of a novel FRP-encased steel-concrete composite column, Compos. Struct. 93 (5) (2011) 1463-73, http://dx.doi.org/10.1016/j.compstruct.2010.11.017.

[18] K. Karimi, W.W. El-Dakhakhni, M.J. Tait, Performance enhancement of steel columns using concrete-filled composite jackets, J. Perform. Constr. Facil. 25(3) (2011) 189-201, http://dx.doi.org/10.1061/(asce)cf.1943-5509.0000162.

[19] K. Karimi, M.J. Tait, W.W. El-Dakhakhni, Influence of slenderness on the behavior of a FRP-encased steel-concrete composite column, J. Compos. Constr. 16 (2012) 100-9, http://dx.doi.org/10.1061/(asce)cc.1943-5614.0000235.

[20] K. Karimi, M.J. Tait, W.W. El-Dakhakhni, Analytical modeling and axial load design of a novel FRP-encased steel-concrete composite column for various slenderness ratios, Eng. Struct. 46 (2013) 526-34, http://dx.doi.org/10.1016/j.engstruct.2012.08.016.

[21] F.M. Ren, Y.W. Liang, J.C.M. Ho, M.H. Lai, Behaviour of FRP tube-concrete-encased steel composite columns, Compos. Struct. 241 (2020) 112139, http://dx.doi.org/10.1016/j.compstruct.2020.112139.

[22] H.X. Zhang, S.L. Ju, H. Chen, Seismic performance of GFRP tube concrete-encased steel composite columns under axial compression, J. Constr. Steel. Res. 200 (2023) 107641, http://dx.doi.org/10.1016/j.jcsr.2022.107641.

[23] L. Wang, B. Chen, Steel reinforced concrete-filed glass fiber reinforced polymer or steel tubular structures, Liaoning Science and Technology Press, Shenyang, China, 2013, pp. 125–131 (in Chinese).

[24] T.M. Pham, H. Hao, Axial impact resistance of FRP-confined concrete, J. Compos. Construct. 21 (2) (2017) 04016088, http://dx.doi.org/10.1061/(ASCE)CC.1943-5614.0000744

[25] L. Huang, X. Sun, L. Yan, B. Kasal, Impact behavior of concrete columns confined by both GFRP tube and steel spiral reinforcement, Construct. Build. Mater. 131 (2017) 438-448, http://dx.doi.org/10.1016/J.CONBUILDMAT.2016.11.095

[26] J. Wang, H.T. GangaRao, R.F. Liang, W.Q. Liu, Experimental and analytical responses of Hollow and concrete-filled GFRP tube columns under Impact, J. Compos. Constr. (2017) 04017013, http://dx.doi.org/10.1061/(ASCE)CC.1943-5614.0000793

[27] Z. Chen, J. Wang, J.Y. Chen, H.T. GangaRao, R.F. Liang, W.Q. Liu, Responses of concrete-filled FRP tubular and concrete-filled FRP-steel double skin tubular columns under horizontal impact, Thin-Walled Struct. 155 (3) (2020) 106941, http://dx.doi.org/10.1016/j.tws.2020.106941.

[28] Y. Qasrawi, P.J. Heffernan, A. Fam, Dynamic behaviour of concrete filled FRP tubes subjected to impact loading, Eng. Struct. 100 (2015) 212-225, http://dx.doi.org/10.1016/j.engstruct.2015.06.012.

[29] O.I. Abdelkarim, M.A. ElGawady, Performance of hollow-core FRP-concrete-steel bridge columns subjected to vehicle collision, Eng. Struct. 123 (2016) 517-531, http://dx.doi.org/10.1016/j.engstruct.2016.05.048.

[30] O.I. Abdelkarim, M.A. ElGawady, Dynamic and static behavior of hollow-core FRP-concrete-Steel and reinforced concrete bridge columns under vehicle collision, Polymers. 8 (12) (2016) 432, http://dx.doi.org/10.3390/polym8120432.

[31] R. Wang, L.H. Han, Z. Tao, Behavior of FRP–concrete–steel double skin tubular members under lateral impact: experimental study, Thin-Walled Struct. 95 (2015) 363-73, http://dx.doi.org/10.1016./j.tws.2015.06.022.

[32] W.Q. Wang, C.Q. Wu, Y. Yu, J.J. Zeng, Dynamic responses of hybrid FRP-concrete-steel double-skin tubular column (DSTC) under lateral impact, Structures. 32 (2021) 1115-1144, http://dx.doi.org/10.1016/j.istruc.2021.02.062.

[33] B. Zhang, S.H. Lin, S.M. Zhang, Y.E. Jiang, C.C. Lai, X.Z. Fu, FRP-concrete-steel tubular columns with a large inner void under lateral impact loading: Experimental study and finite-element modelling, J. Buil. Eng. 80 (2023) 108006, https://doi.org/10.1016/j.jobe.2023.108006.

[34] R. Wang, L.H. Han, C.C. Hou, Behavior of concrete filled steel tubular (CFST) members under lateral impact: experiment and FEA model, J. Constr. Steel Res. 80 (2013) 188-201, http://dx.doi.org/10.1016/j.jcsr.2012.09.003.

[35] S. Gao, Y. Xu, S.M. Zhang, A. Derlatka, Performance of square concrete-filled steel tubular columns under repeated lateral impact, Eng. Struct. 280 (2023) 115719, http://dx.doi.org/10.1016/j.engstruct.2023.115719.

[36] W.Q. Wang, C.Q. Wu, J. Li, Z.X. Liu, Y.P Lv, Behavior of ultra-high performance fiber reinforced concrete (UHPFRC) filled steel tubular members under lateral impact loading, Int. J. Impact Eng. 132 (2019) 103314, https://doi.org/10.1016/j. ijimpeng.2019.103314.

[37] Murray YD. Users manual for LS-DYNA concrete material model 159. McLean, VA: Department of Transportation; 2007.

[38] G. Gholipour, A.M. Billah, Dynamic behavior of bridge columns reinforced with shape memory alloy rebar and UHPFRC under lateral impact loads, Int. J. Impact Eng. 168 (2022) 104297, https://doi.org/10.1016/j.ijimpeng.2022.104297.

[39] C.C. Hou, L.H. Han, F.C. Wang, C.M. Hu, Study on the impact behaviour of concrete encased CFST box members, Eng. Struct. 198 (2019), 109536, https://doi.org/ 10.1016/j.engstruct.2019.109536.

[40] A.A. Mutalib, H. Hao H, Development of PI diagrams for FRP strengthened RC columns, Int. J. Impact. Eng. 38 (2011) 290-304, http://dx.doi.org/10.1016/j.ijimpeng.2010.10.029.

[41] W.C. Zhao, J.H. Ye, Dynamic behavior and damage assessment of RC columns subjected to lateral soft impact, Eng. Struct. 251 (2022) 113476, https://doi.org/10.1016/j.engstruct.2021.113476.

[42] G.C. Li, J.L. Wang, C. Fang, X. Li, Y. Zhou, Performance of CFST members internally strengthened with I-shaped CFRP under impact load, J. Constr. Steel Res. 211 (2023) 108132, https://doi.org/10.1016/j.jcsr.2023.108132.

[43] Q.J. Wu, X.D. Zhi, Q.X. Li, M.H. Guo, Experimental and numerical studies of GFRP-reinforced steel tube under low-velocity transverse impact, Int. J. Impact. Eng. 127 (2019) 135-153, http://dx.doi.org/10.1016/j.ijimpeng.2019.01.010

[44] QC/T 487-2009, China Planning Press, Beijing, 2009. (in Chinese)

[45] H. Sharma; S. Hurlebaus; P. Gardoni, Performance-based response evaluation of reinforced concrete columns subject to vehicle impact, Int. J. Impact Eng. 43 (2012), 52-62, http://dx.doi.org/10.1016/j.ijimpeng.2011.11.007

[46] W.T. Xie, Y. Chen, S.H. Han, W.B. Zhou, Research on I steel reinforced concrete-filled GFRP tubular short columns, Thin-Walled Struct. 120 (2017) 282-296, http://dx.doi.org/10.1016/j.tws.2017.08.031.

[47] GB/T 706-2016, Hot rolled section steel China standard Press, Beingjing, 2016. (in Chinese)